

Contents lists available at ScienceDirect

# Computers and Fluids

journal homepage: www.elsevier.com/locate/compfluid





# Optimized Filters for Stabilizing High-Order Large Eddy Simulation

Mohsen Hamedi\*, Brian C. Vermeire

Department of Mechanical, Industrial, and Aerospace Engineering, Concordia University, Montreal, QC, Canada

#### ARTICLE INFO

Keywords: Stabilization Filtering High-order Flux Reconstruction Large Eddy Turbulence

#### ABSTRACT

High-order Flux Reconstruction (FR) schemes can be used to simulate unsteady turbulent flows using Large Eddy Simulation (LES) and Direct Numerical Simulation (DNS) in the vicinity of complex geometries. However, the application of FR can be limited by non-linear instabilities, which can arise from oscillatory behaviour of the underlying polynomial representation of the solution. In this paper, we explore filtering and its parametrization for stabilizing under-resolved simulations of the Navier–Stokes equations. A new exponential filtering operator is proposed, which is normalized by the time-step size and designed to filter high-frequency modes. Over 14,000 numerical tests are then performed to obtain an optimal set of filtering parameters, with the objective being to stabilize while maintaining high-order accuracy. We then verify that these optimal filters converge to super-accuracy for non-linear problems, and compare filtered and unfiltered simulations of the Taylor–Green vortex using both straight and curved meshes, and turbulent channel flow. These demonstrate that the filtered solutions are generally more accurate than unfiltered ones, while still stabilizing previously unstable simulations. Finally, we demonstrate the utility of these filters for more complex flows, specifically a stalled NACA 0020 airfoil

methods are based on the integral form of the governing equations and SD is based on the differential form. Recently, Huynh [22] introduced the FR approach, which is a single framework capable of recovering existing schemes such as DG [23], SV, and SD, and also formulating new schemes with different stability and accuracy properties [24]. Similar to SD, FR is derived via the differential form of the governing equations. The FR approach has proven to be accurate for scale-resolving simulations, such as DNS, LES, and Implicit LES (ILES) [25,26] for complex unsteady turbulent flows [27–31]. In the case of ILES, the numerical dissipation of the FR approach acts as a built-in Sub-Grid Scale (SGS) model [25,26] in conjunction with appropriate high-order time-stepping approaches [32,33].

While the utility of high-order methods, such as DG, SV, SD, and FR, have been demonstrated for scale-resolving LES/DNS, their non-linear stability properties are typically less robust than those of lower-order methods. High-order schemes are usually more sensitive to numerical instabilities due to their relatively low numerical dissipation. These numerical instabilities, mainly arising from non-linear behaviour of the governing equations, can be dealt with using different techniques. Aliasing error discussed by Phillips [34], is known as one of the sources of instability in non-linear problems, which arises in the projection of the flux polynomial into a lower-dimensional space. In DG and FR methods, a finite set of basis functions is used to construct a numerical solution within each cell. Applying these methods to nonlinear equations can generate these so-called aliasing errors, where the unresolved modes are aliased into lower modes [5]. Kirby and Karniadakis [35] introduced de-aliasing for unstructured grids. Spiegel, Huynh, and DeBonis [5] studied over-integration, as a de-aliasing technique, for FR using LES, and showed that over-integration reduces aliasing error. Jameson et al. [36] showed that by employing an exact L2 projection, instead of a collocation projection, to construct the approximation of the flux polynomial, aliasing-driven instabilities will be eliminated; however, performing an L2 projection is more expensive in terms of the computational cost. Entropy stable schemes can also be used to deal with non-linear instabilities; however, constructing such schemes is generally challenging and computationally expensive [37]. In problems containing shock waves, a shock-capturing method can be used. Persson and Peraire [38] introduced a shock-capturing method for DG inspired by the early artificial viscosity methods [39]. Burbeau, Sagaut, and Bruneau [40] introduced a problem independent limiter capable of capturing strong shocks while preserving the accuracy of the DG method in smooth regions. Another approach to stabilization is filtering, which aims to damp spurious oscillations that arise due to aliasing, discontinuities, or under-resolution. Trojak et al. [41] have studied the effects of filtering on both semi- and fully-discrete schemes, showing the effectiveness of filtering in temporal stabilization with a mild reduction in the order of accuracy of the method. Recently, Park et al. [42] compared modal filtering [43] and de-aliasing [44] on highorder ILES of a flow over a NACA0021 airfoil. They concluded that filtering degrades solution accuracy; however, its computational cost is significantly less than de-aliasing. In summary, different instabilities require different stabilization techniques. For example, limiters and/or artificial dissipation can be used to stabilize shocks/discontinuities, and instabilities resulting from under-resolved simulations can be dealt with using de-aliasing and/or filtering techniques. These techniques might be used in combination when different instabilities are observed, or additional stabilization is required. Hence, popular stabilization techniques include de-aliasing, limiters, artificial dissipation, and filtering, among which the first two have relatively high computational cost. De-aliasing utilizes more quadrature points to approximate the flux function more accurately. Limiters need to evaluate a set of predefined slopes to find the troubled elements to limit cell averages. And artificial dissipation, being a competitor to filtering in terms of computational cost, needs a sensor to find discontinuities and damp spurious oscillations. This sensor is an additional cost since it requires integration over an element for the indicator, depending on whether this is performed

every Runge–Kutta stage or once per time-step [38]. In contrast, filtering typically has negligible computational cost. However, as shown by Park et al. [42], it can have detrimental effects on accuracy. Hence, it remains to be shown whether filtering operators can be designed such that they stabilize the solution, while maintaining accuracy.

The objective of this research is to introduce a new accuracy preserving filtering technique for stabilization of high Reynolds number flows using high-order spatial discretizations. In Section 2, FR is explained, and filtering is discussed in Section 3. These filters are then optimized to maintain stability in the context of the TGV at an infinite Reynolds number. Then, the super-accuracy of these optimal filters is verified via non-linear isentropic vortex advection in Section 4, and these optimized filters are validated for a set of benchmark LES cases in Section 5. These include ILES of the TGV, turbulent channel flow, and a stalled NACA0020 airfoil. Finally, conclusions and recommendations for future work are given in Section 6.

#### 2. Flux Reconstruction

The FR approach, a high-order accurate numerical method first introduced by Huynh [22], is appealing due to its accuracy, generality, robustness, and suitability for modern hardware architectures [2]. In comparison to common low-order numerical methods, FR provides more accurate solutions using fewer total number of Degrees of Freedom (DoF) at a reduced computational cost [3]. As mentioned previously, FR is a unifying approach that can recover existing schemes such as the SD, SV, and DG methods, for linear equations. As with the SD and DG approaches, FR makes use of a high-order polynomial basis to represent the solution on each element. The one-dimensional formulation of the FR framework is explained here, along with its extension to multiple dimensions [45].

#### 2.1. One-dimensional formulation

Consider a 1D general conservation law of the form

$$\frac{\partial u}{\partial t} + \frac{\partial f}{\partial x} = 0,\tag{1}$$

where u=u(x,t) is the conserved scalar quantity, t is time, f=f(u) is the flux of u in the x direction, and x is the spatial coordinate. The computational domain,  $\Omega$ , is partitioned into a mesh of  $N_e$  non-overlapping elements such that

$$\Omega = \bigcup_{k=1}^{N_e} \Omega_k, \qquad \bigcap_{k=1}^{N_e} \Omega_k = \emptyset, \tag{2}$$

where  $\Omega_k = \{x \mid x_k^- < x < x_k^+\}$ , and  $x_k^-$  and  $x_k^+$  are the left and right boundaries of  $\Omega_k$ , respectively. The exact solution, u, is approximated initially within each element via a solution polynomial of degree  $\mathcal{P}$ , interpolated using a set of  $N_p = \mathcal{P} + 1$  discrete solution points. Similarly, the exact flux, f, within each element,  $\Omega_k$ , is approximated by a flux polynomial of degree  $\mathcal{P} + 1$ , that is continuous across cell interfaces. Hence, the total numerical solution,  $u^\delta$ , and flux,  $f^\delta$ , can be represented as the direct sum of their element-wise approximations  $u_k^\delta$  and  $f_k^\delta$ ,

$$u \approx u^{\delta} = \bigoplus_{k=1}^{N_e} u_k^{\delta}, \qquad f \approx f^{\delta} = \bigoplus_{k=1}^{N_e} f_k^{\delta}.$$
 (3)

The solution polynomial within each element is interpolated using nodal basis functions, ensuring element-wise continuity of the solution,

$$u_k^{\delta}(x,t) = \sum_{i=1}^{N_p} u_{k,i}^{\delta} \phi_i(x), \tag{4}$$

where  $u_{k,i}^{\delta}$  is the numerical solution at point i within element  $\Omega_k$ , and  $\phi_i(x)$  is the nodal basis function at point i. The nodal basis functions in 1D are the well-known Lagrange polynomials, shown in Fig. 1 and defined as

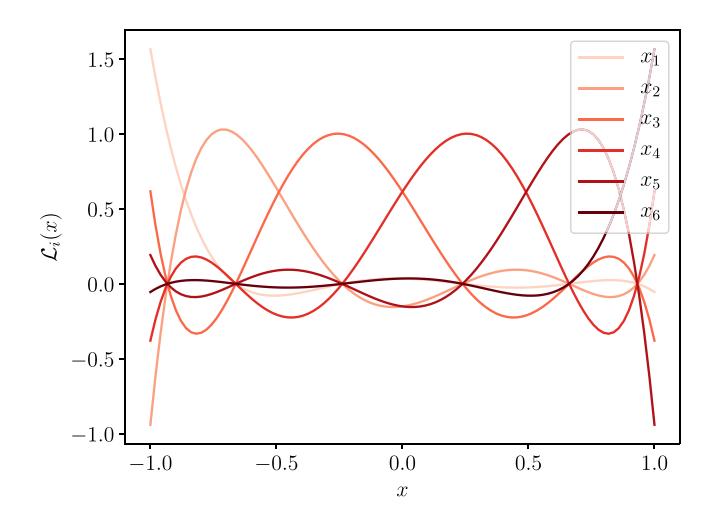


Fig. 1. Lagrange polynomials for P=5 using Gauss points, in a reference element  $\begin{bmatrix} -1 & 1 \end{bmatrix}$ 

$$\mathcal{L}_{i}(x) = \prod_{i=1, i \neq i}^{N_{p}} \frac{x - x_{j}}{x_{i} - x_{j}}.$$
 (5)

The flux at every point is computed using the approximate value of the solution at that point, i.e.,  $f_{k,i}^{\delta} = f\left(u_{k,i}^{\delta}\right)$ . In the case of nonlinear conservation laws, the flux polynomial is approximated using the Lagrange interpolation polynomial,

$$f_k^{\delta D}(x,t) = \sum_{i=1}^{N_p} f_{k,i}^{\delta} \mathcal{L}_i(x), \tag{6}$$

where  $f_{k,i}^\delta=f\left(u_{k,i}^\delta\right)$  is the numerical flux value at point i within element  $\Omega_k$ .

The constructed numerical flux function,  $f_{\delta}^{\delta D}(x,t)$ , is generally discontinuous across cell interfaces, and the superscript D denotes this discontinuity. The flux function is required to be continuous across cell interfaces to satisfy conservation [24]. To address this discontinuity of flux function, Huynh [22] proposed a reconstruction for the flux function. The new reconstructed and continuous flux function must be of degree P+1. Therefore, its spatial derivative will be in the same polynomial space as the temporal derivative of the numerical solution polynomial. The reconstructed flux polynomial must approximate  $f_{\delta}^{D}(x,t)$ , and at the interfaces of each element must take on the value of common Riemann fluxes, i.e.,

$$f_{k}^{\delta}(x_{k}^{-}) = f^{R}(u_{k-1}^{\delta}(x_{k}^{-}), u_{k}^{\delta}(x_{k}^{-})) \equiv f_{k}^{R-}, \tag{7}$$

$$f_k^{\delta}\left(x_k^+\right) = f^R\left(u_k^{\delta}\left(x_k^+\right), u_{k+1}^{\delta}\left(x_k^+\right)\right) \equiv f_k^{R+},\tag{8}$$

where  $f^R\left(u^-,u^+\right)$  is an appropriate Riemann flux, a function of extrapolated values of the numerical solution at each edge of neighbouring elements. In what follows, the dependence on time is dropped for simplicity of notation. The reconstructed flux is

$$f_k^{\delta}(x) = f_k^{\delta D}(x) + f_k^{c}(x), \tag{9}$$

where  $f_{k}^{c}(x)$  is a correction flux polynomial, defined as

$$f_{L}^{c}(x) = \left(f_{L}^{R-} - f_{L}^{\delta D}(x_{L}^{-})\right) g_{L}(x) + \left(f_{L}^{R+} - f_{L}^{\delta D}(x_{L}^{+})\right) g_{R}(x). \tag{10}$$

The flux correction should be close to zero in the interior of each element, and  $g_L(x)$  and  $g_R(x)$  are the correction functions, which must satisfy the following constraints

$$g_L(x_k^-) = 1, \quad g_L(x_k^+) = 0,$$
 (11)

$$g_R(x_k^-) = 0, \quad g_R(x_k^+) = 1.$$
 (12)

To advance the numerical solution in time, the following differential equation must be solved

$$\frac{\partial u_k^{\delta}}{\partial t} + \frac{\partial f_k^{\delta}}{\partial x} = 0. \tag{13}$$

Substituting the Eqs. (9) and (10) into (13) yields in

$$\frac{\partial u_{k}^{\delta}}{\partial t} + \frac{\partial f_{k}^{\delta D}}{\partial x} + \left(f_{k}^{R-} - f_{k}^{\delta D}\left(x_{k}^{-}\right)\right) \frac{\partial g_{L}(x_{k})}{\partial x} + \left(f_{k}^{R+} - f_{k}^{\delta D}\left(x_{k}^{+}\right)\right) \frac{\partial g_{R}(x_{k})}{\partial x} = 0. \tag{14}$$

As stated earlier, FR is a single framework capable of recovering various schemes. There are three factors that FR relies on for such a property. The location of the solution points, the approximate Riemann solver in obtaining the common interface fluxes,  $f_k^{R-}$  and  $f_k^{R+}$ , and the choice of the correction functions,  $g_R$  and  $g_L$ . The choice of the solution point locations plays a key role in the stability and accuracy properties of the scheme when the flux is non-linear. However, in the case of linear fluxes, it only affects initial projection error when using a collocation projection of the initial condition onto polynomial space [46]. The choice of Riemann solver influences the amount of numerical dissipation introduced by the spatial discretization. In the context of ILES, this dissipation is responsible for reducing or eliminating a pile-up of kinetic energy in high-frequency modes. In this study, we use a Rusanov/Lax-Friedrichs flux at the interface between elements and note that previous work has explored the properties of different Riemann solvers in this context [47]. Hence, it is important to note that the filters proposed in this study may not be optimal for different Riemann solvers. Depending on the choice of correction function, one can recover the DG, SD, and SV methods, or continuous families of linearly stable schemes [22]. Huynh [22] showed that by choosing  $g_L$  and  $g_R$  as the right and left Radau polynomials, the collocation based nodal DG scheme will be recovered, which is the scheme used in the current study.

# 2.2. Lifting Collocation Penalty Formulation

The FR framework can also extend to multiple dimensions using the Lifting Collocation Penalty (LCP) formulation [45]. Consider the general form of a hyperbolic conservation law

$$\frac{\partial u}{\partial t} + \nabla \cdot \mathbf{f}(u) = 0. \tag{15}$$

A weighting function, W, is defined to ensure a unique solution exists for Eq. (15). Following the FR approach [22] and its extension to simplex element types [45], Eq. (15) is re-written as

$$\frac{\partial u_k^{\delta}}{\partial t} + \nabla \cdot \boldsymbol{f}_k^{\delta} + \vartheta_k = 0, \tag{16}$$

where  $\theta_k$  is a correction field on the element  $\Omega_k$ . The correction field is analogous to the divergence of the correction functions in the FR approach, which enforces continuity of the flux polynomial across element interfaces.

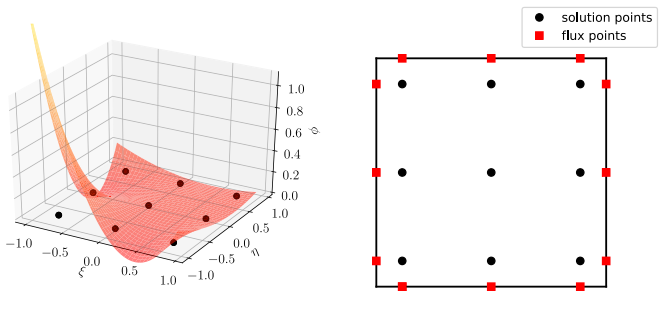
Eq. (16) must be satisfied at each solution point,  $x_{k,i}$ , i.e.,

$$\frac{du_{k,i}^{\delta}}{dt} + \left(\nabla \cdot \boldsymbol{f}_{k}^{\delta}\right)_{\mathbf{x}_{k,i}} + \theta_{k,i} = 0, \tag{17}$$

where for elements with straight faces

$$\theta_{k,i} = \frac{1}{|\Omega_k|} \sum_{\sigma \in \partial \Omega_i} \sum_i \alpha_{i,\mathcal{F},j} \left[ f^R \right]_{\mathcal{F},j} S_{\mathcal{F}}, \tag{18}$$

where  $\mathcal F$  denotes the faces of the element  $\Omega_k$ , j is the index for flux points,  $\alpha_{i,\mathcal F,j}$  are constant lifting coefficients,  $\left[f^R\right]_{\mathcal F,j}$  is the difference between a common Riemann flux at point j and the value of the internal flux, and  $S_{\mathcal F}$  is the area of the face  $\mathcal F$ . The lifting coefficients are computed using  $\mathcal W$ , and are independent of both geometry and the solution. A number of different energy stable schemes, such as SD, SV, and DG, can be recovered based on the specification of these



(a) Nodal basis function at one solution point,

(b) The solution and flux points

Fig. 2. Orthonormal basis function and solution and flux points for quadrilateral element types and  $\mathcal{P}=2.$ 

lifting coefficients. In this study, DG is recovered by using the lifting coefficients based on the nodal basis functions.

In order to make FR simpler and more efficient, all operations are commonly performed in a reference space, and all elements,  $\Omega_k$ , are transformed from the physical domain  $\boldsymbol{x}$  to this standard reference space  $\boldsymbol{\xi}$ , using a one-to-one mapping function, M, as

$$\mathbf{x} = M(\xi), \qquad \xi = M^{-1}(\mathbf{x}). \tag{19}$$

A nodal polynomial representation of degree  $P_m$  of the mapping function, M, is defined, using the mapping points

$$\mathbf{x}_{k}^{\delta}(\xi) = \sum_{i}^{N_{m}} x_{k,i} \phi_{m,k,i}(\xi), \qquad (20)$$

where  $\mathbf{x}_k^{\delta}(\boldsymbol{\xi})$  is the interpolated physical location,  $N_m$  is the number of mapping points, and  $x_{k,i}$  is the physical location of the mapping points. The Jacobian determinant of this transformation at any point is

$$J = \left| \frac{\partial \mathbf{x}}{\partial \xi} \right|. \tag{21}$$

Aliasing errors are mainly due to either the non-linearity of the equations or mapping curved elements into the reference space [48]. In the case of curved elements, the Jacobian of the isoparametric mapping is a non-constant, non-linear polynomial, which introduces a geometrical-aliasing source [44].

The solution and flux polynomials are interpolated, similar to 1D formulation, using the nodal basis functions. An example of nodal basis function for a quadrilateral element is shown in Fig. 2, along with the locations of solution and flux points of the same element.

## 3. Filtering

#### 3.1. Polynomial representation

Polynomials can be represented in different equivalent forms, including nodal and modal. Nodal in a sense that the polynomial is built using the value of the solution at nodes, and modal in a sense of orthogonal polynomial modes. The general form of these representations of the solution, omitting the element index for brevity, is

$$u^{\delta}(\boldsymbol{\xi},t) = \sum_{i=1}^{N_p} u_i^{\delta}(t)\phi_i(\boldsymbol{\xi}), \tag{22}$$

$$u^{\delta}(\boldsymbol{\xi},t) = \sum_{i=1}^{N_p} \hat{u}_i^{\delta}(t)\psi_i(\boldsymbol{\xi}), \tag{23}$$

where  $u_i^\delta$  is the nodal coefficient or the numerical solution values at each solution point in the reference space,  $\hat{u}_i^\delta$  is the *i*th modal coefficient,  $\phi_i(\xi)$  is the nodal basis function at the *i*th solution point, and  $\psi_i(\xi)$  is the *i*th orthonormal basis function. These orthonormal basis functions can be written as a weighted summation of monomial terms

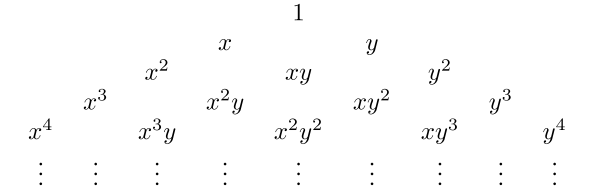


Fig. 3. Pascal's triangle for two dimensional elements.

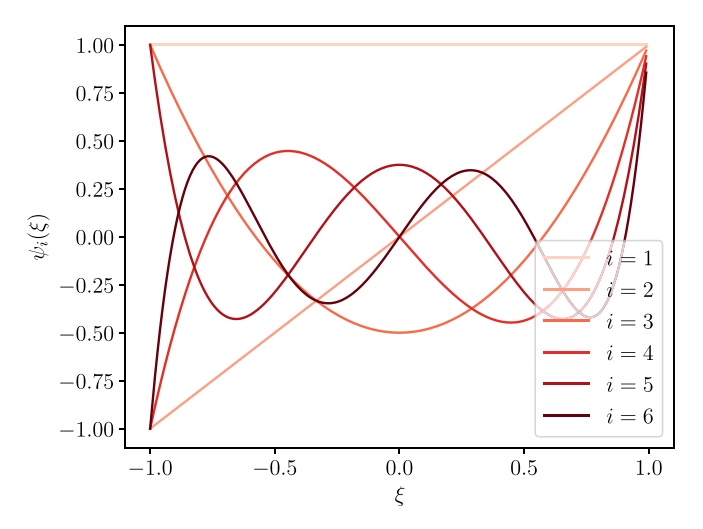


Fig. 4. Legendre polynomials for P = 5 in a reference element [-1, 1].

from Pascal's triangle, shown in Fig. 3. In the 1D case, the nodal and orthonormal basis functions are the well-known Lagrange and Legendre polynomials, respectively. These polynomials are shown in Figs. 1 and 4 for  $\mathcal{P}=5$ . Example 2D orthonormal modal basis functions are also shown in Fig. 5.

To switch back and forth between these two polynomial representations, the Vandermonde matrix is used

$$\boldsymbol{u}^{\delta} = V\hat{\boldsymbol{u}}^{\delta},\tag{24}$$

$$\hat{\boldsymbol{u}}^{\delta} = V^{-1} \boldsymbol{u}^{\delta},\tag{25}$$

where  $\mathbf{u}^{\delta}$  and  $\hat{\mathbf{u}}^{\delta}$  are the vector of nodal and modal coefficients, respectively, and V is the Vandermonde matrix, which is defined as [43]

$$V_{ij} = \psi_i(\xi_i), \tag{26}$$

where  $\psi_j(\xi_i)$  is the *j*th orthonormal basis function evaluated at the *i*th solution point.

# 3.2. A time-step independent filtering operator

The modal form of representing a polynomial is analogous to a Fourier series, where the higher modes are responsible for the oscillatory behaviour of that polynomial, as seen in Fig. 4. In order to stabilize a simulation, spurious oscillations of the numerical solution should be damped. Hence, a filtering operator can be applied to the vector of modal coefficients, to reduce the energy of the higher modes. The decay of the expansion coefficients,  $\hat{\boldsymbol{u}}^{\delta}$ , has a relation with the accuracy of the scheme, and proper selection of these coefficients can improve accuracy [49]. In the FR approach, the desired form of a polynomial representation is the nodal form. Thus, the filtering operator should be defined such that it filters the modal coefficients and returns the filtered nodal coefficients. This filtering operation can be cast as [43]

$$F = V\Lambda V^{-1},\tag{27}$$

where  $\Lambda$  is a modal filtering matrix, which is defined in the next section. Using this definition, switching back and forth between different forms

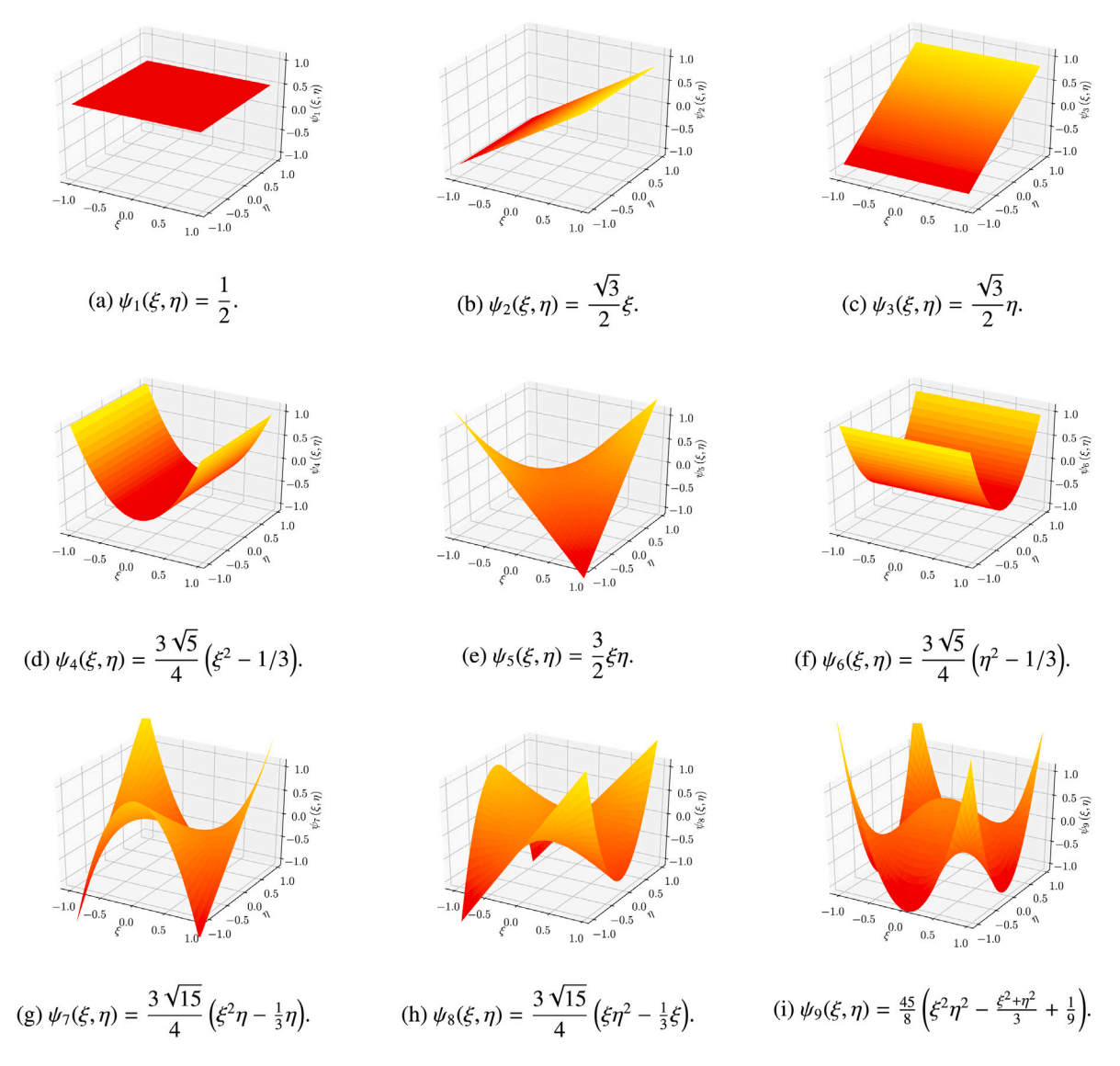


Fig. 5. The orthonormal modal basis functions in 2D for quadrilateral elements and P = 2.

of polynomial representations is done in a single operation via the filtering matrix F.

The filtering operator is typically applied after each time-step, making the observed filter strength dependent on the time-step size. Thus, changing the size of the time-step results in a different observed strength of the filtering over a fixed time interval. This makes the selection of an appropriate modal filter case dependent. To avoid this, we propose a new filtering operator whose strength is normalized by the time-step size. The normalized form of the  $\Lambda$  matrix is

$$\Lambda^* = \Lambda^{\frac{1}{n}},\tag{28}$$

where n is

$$n = \frac{T_{char}}{\Delta t},\tag{29}$$

where  $T_{char}$  is a characteristic time relevant to the flow of interest, and  $\Delta t$  is the time-step size. Therefore, the filtering operator normalized by the time-step size will be

$$F^* = V\Lambda^*V^{-1}. (30)$$

In the conventional filtering approach, F is applied after each timestep, making the cumulative filtering strength over a fixed simulation time dependent on the time-step size. The proposed filtering operator,  $F^*$ , is also applied after each time-step; however, its strength is normalized by the time-step size. Thus, applying  $F^*$  after each time-step for n times is analogous to applying F after each characteristic time,  $T_{char}$ , only once, eliminating the time-step dependence of the proposed filter. Hence, the observed filter strength remains constant, no matter the time-step size,  $\Delta t$ . The spectral properties of a fully-discrete scheme are dependent on both space and time discretizations. However, provided the temporal integration is of a sufficiently high order, and the time-step is not in the vicinity of the stability limit, the behaviour of the scheme is primarily governed by the spatial operator [33]. Thus, the proposed formulation is independent of the temporal integration scheme, provided the integration meets the aforementioned conditions. Otherwise, the following optimization might yield different parameters.

# 3.3. Filtering matrix

The modal filtering matrix is a square diagonal matrix with filtering function values on its main diagonal, defined as

$$\Lambda_{ii} = \sigma(\eta), \qquad i = 1, \dots, N_p \tag{31}$$

where  $\sigma$  is the filtering function and  $\eta$  is the summation of the exponents of the highest degree term of the corresponding orthonormal basis function, obtained using Pascal's triangle. To find the aforementioned terms in 3D, Pascal's triangle is used in multiple layers.

The commonly used exponential filtering function [43] is used in this study which is defined as

$$\sigma(\eta) = \begin{cases} 1 & 0 \le \eta \le \eta_c \\ exp\left(-\alpha \left(\frac{\eta - \eta_c}{\eta_{max} - \eta_c}\right)^s\right) & \eta_c \le \eta \le \eta_{max} \\ 0 & \eta > \eta_{max} \end{cases}$$
(32)

where  $\alpha$  and s are the damping and strength parameters of the filter function, respectively,  $\eta_{max}$  is the maximum summation of the exponents of the orthonormal basis, and  $\eta_c$  is the cut-off degree. In order to reduce the effects of filter on the convergence rate, the smoothness of the filtering function must exceed that of the solution [49]. Thus, the exponential filter function is an appealing choice. The relation between these filtering parameters is shown in Fig. 6, where  $\eta^* = \eta/\eta_{max}$ . It can be seen that the filtering function will move towards higher degrees by increasing the values of s and/or  $\eta_c$  and decreasing  $\alpha$ .

#### 3.4. Parameter optimization

The strength of the filter is dependent on the choice of s,  $\eta_c$ , and  $\alpha$ . Excessive filtering will reduce accuracy, while insufficient dissipation will fail to stabilize the solution. To find suitable filtering parameters, the Taylor–Green Vortex (TGV) has been studied in the limit of an infinite Reynolds number. In the TGV problem, the Navier–Stokes equations are solved in 3D to simulate a freely decaying turbulent flow in a periodic domain, generating a detailed turbulent spectrum. The initial flow field for the TGV is specified as [24]

$$u = +U_0 \sin(x/L)\cos(y/L)\cos(z/L), \tag{33}$$

$$v = -U_0 \cos(x/L) \sin(y/L) \cos(z/L), \tag{34}$$

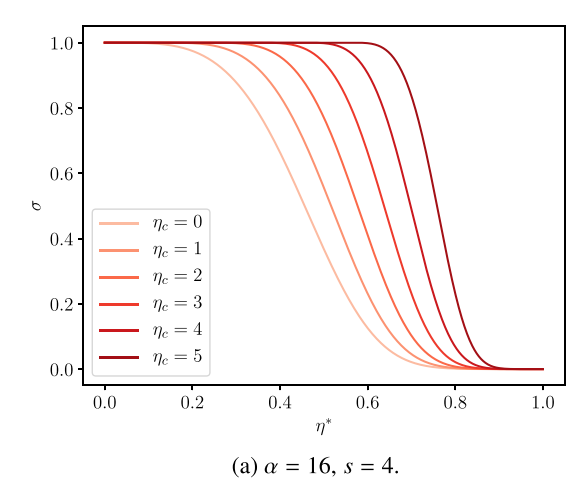
$$w = 0, (35)$$

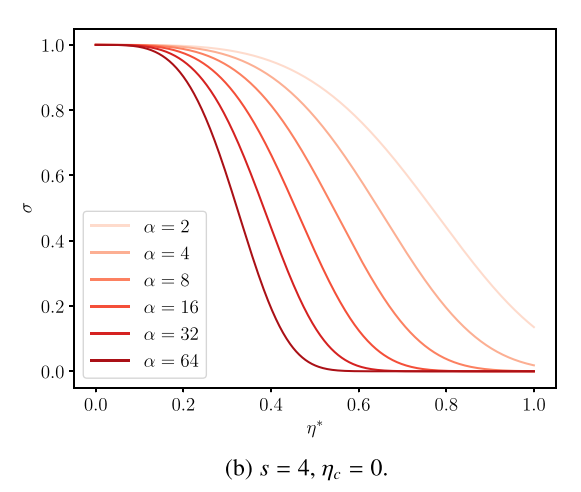
$$P = P_0 + \frac{\rho_0 U_0^2}{16} \left(\cos(2x/L) + \cos(2y/L)\right) \left(\cos(2z/L) + 2\right),\tag{36}$$

$$\rho = \frac{P}{RT_0},\tag{37}$$

where u, v, and w are the velocity components, P is the pressure,  $\rho$  is the density, and L=1 is the characteristic length. The constant values of characteristic velocity,  $U_0$ , and temperature,  $T_0$ , are specified to have the desired flow Mach number.

In this section, the TGV is used to explore stability in the limit of infinite Reynolds number, so the Euler equations are used in lieu of Navier–Stokes, with solution polynomials of degree P = 3, 4, and 5. The domain for this study is a periodic cube with dimensions of  $0 \le x, y, z \le$  $2\pi L$ , meshed with hexahedral elements, and the total number of DoF is 16<sup>3</sup>. A very coarse mesh is used to have an initially unstable simulation, and the filtering operator is applied using a wide range of filtering parameters. There are three tuning parameters in the filtering operator, as shown in Eq. (32). To optimize the filtering operator, we attempt to find a set of filtering parameters that can be used for general flows, alleviating the need to tune these parameters. The strength parameter is set to fixed values of s = [2, 4, 8, 16] throughout this study. As mentioned earlier, we are interested in filtering the highest orders of the solution polynomial. Thus, the cut-off degree,  $\eta_c$ , is set equal to the maximum summation of the exponents of the orthonormal basis,  $\eta_{max}$ . Then, as the first step, using Algorithm 1, the highest possible  $\eta_c$  is found for a very large value of  $\alpha$  that stabilizes the simulation. Following this, finding the lower and upper bounds of the damping parameter  $\alpha$  is the second step. This step is done using Algorithms 2 and 3. Finally, the last step is to find the optimized value of  $\alpha$ , using the bisection method shown in Algorithm 4. The optimized values of  $\eta_c$  and  $\alpha$  are found by running more than 14000 simulations using bisection over the aforementioned range of parameter s, solution polynomial degrees, and Mach numbers. The damping parameter,  $\alpha$ , is optimized to have the weakest filtering operator, to preserve accuracy, while stabilizing the TGV simulation. Stability is defined as a solution that maintains physical solutions up





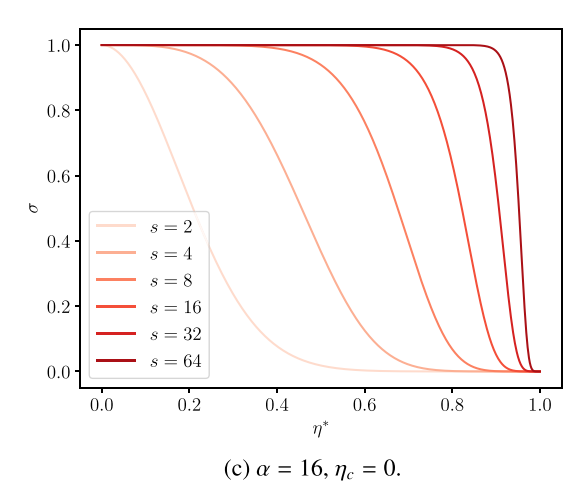


Fig. 6. The effect of different parameters on the filter function.

to  $20T_{char}$ , where a physical solution is interpreted as one having only non-negative and/or non-imaginary values of pressure and density, and  $T_{char} = L/U_0$  is the characteristic time of the TGV. This is studied at different Mach numbers ranging from Ma = 0.1 to 0.5.

The threshold of stability, determined via bisection, for different solution polynomial degrees and Mach number of Ma=0.1 are given in Fig. 7 and for all other Mach numbers are given in Figs. 31–34 in Appendix A. Any value for parameters on the left side of each line in these figures is considered a weak filter that fails at stabilization, while

#### **Algorithm 1:** Finding the maximum possible value of $\eta_c$

```
\alpha = 10^{16}:
for P = [3, 4, 5] do
    for Mach = [0.1, 0.2, 0.3, 0.4, 0.5] do
        for s = [2, 4, 8, 16] do
             \eta_c = \eta_{max};
             stability = 0;
             while stability = 0 do
                 Run TGV Simulation;
                 if TGV Simulation is stable then
                     stability = 1;
                 else
                    \eta_c = \eta_{max} - 1;
                 end
             end
        end
    end
end
```

# **Algorithm 2:** Finding the lower bound of $\alpha$

```
for P = [3, 4, 5] do
    for Mach = [0.1, 0.2, 0.3, 0.4, 0.5] do
        for s = [2, 4, 8, 16] do
             \alpha_l = 10^4;
             stability = 0;
             while stability = 0 do
                 Run TGV Simulation;
                 if TGV Simulation is unstable then
                     \alpha_l = 10\alpha_l;
                 else
                      stability = 1;
                     \alpha_i = \alpha_i/10;
                 end
             end
        end
    end
end
```

# **Algorithm 3:** Finding the upper bound of $\alpha$

```
for P = [3, 4, 5] do
    for Mach = [0.1, 0.2, 0.3, 0.4, 0.5] do
        for s = [2, 4, 8, 16] do
             \alpha_{u} = 10^{16};
             stability = 1;
             while stability = 1 do
                 Run TGV Simulation;
                 if TGV Simulation is stable then
                      \alpha_u = \alpha_u/10;
                 else
                      stability = 0;
                      \alpha_u = 10\alpha_u;
                 end
             end
        end
    end
end
```

parameter values on the right side of each line form a filtering function that stabilizes the simulation.

**Algorithm 4:** Finding the optimum value of  $\alpha$ 

```
for P = [3, 4, 5] do
     for Mach = [0.1, 0.2, 0.3, 0.4, 0.5] do
         for s = [2, 4, 8, 16] do
              define tol;
              while \alpha_u - \alpha_l > tol do
                   \alpha = \frac{1}{2}(\alpha_l + \alpha_u);
                   Run TGV Simulation;
                   if TGV Simulation is stable then
                    \alpha_u = \alpha;
                   else
                    \alpha_l = \alpha;
                   end
              end
         end
    end
end
```

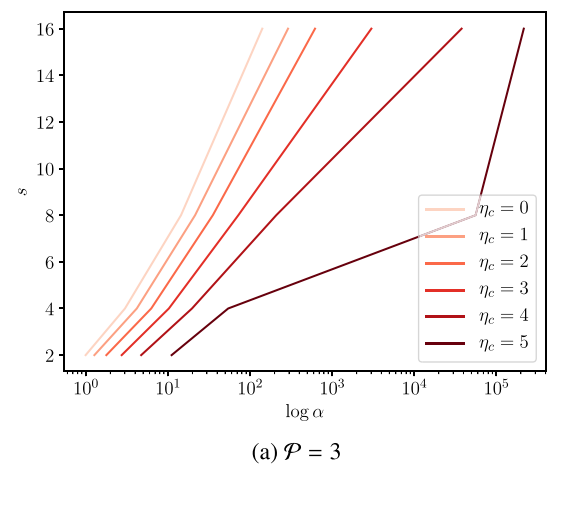
In the available literature, the predominant correction function that is used in FR is the one that recovers the DG scheme. Thus, the DG scheme is chosen in this study, and we note that our filters are optimized specifically for this scheme and would not be generally suitable for other correction functions. Oscillatory behaviour of the solution is typically due to the highest modes in the solution polynomial. Hence, it is beneficial to damp only the higher-order modes if possible. Therefore, low-pass filtering in the spectral domain is preferred [50]. One hypothesis of this work is that, by selectively filtering only the higherorder modes, we may be able to preserve the high-order accuracy of the scheme, which is explored in the next section. Furthermore, it is expected that these higher-order modes are responsible for significant aliasing error since their products are of a much higher polynomial degree than those used to represent the solution. Hence, we consider the best set of filtering parameters as those that damp the higher modes as much as possible while leaving the lower modes unchanged. All of the possible filtering functions for Ma = 0.1 are shown in Fig. 8, where the best filtering function under these criteria is highlighted. These plots for filtering operators at different Mach numbers are shown in Figs. 35-38 in Appendix B, and the corresponding filtering parameters for all of the optimum filter functions of different strengths are given in Tables 4-6 in Appendix C. An interesting correlation is observed from these figures is that the spectrum, in general, is split into 2/3 and as P increases it tends towards 1/2, which is similar to the 2/3 rule of dealiasing [51]. The optimum time-step independent filter function for solution polynomials of degree P = 3, 4, and 5 are determined at different filter strengths ranging from  $\Lambda_{Mach=0.1}$  to  $\Lambda_{Mach=0.5}$ . The proposed filtering functions are verified in the following section.

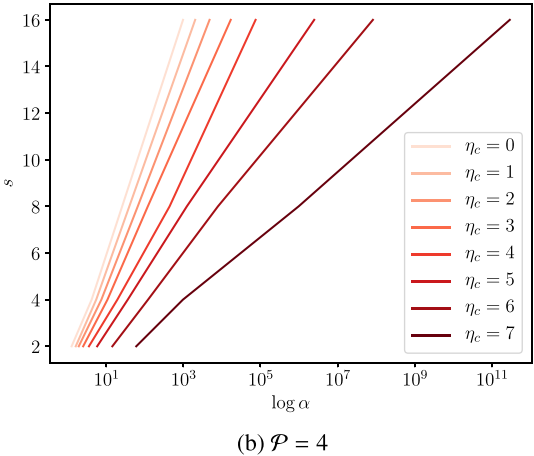
# 4. Verification and validation

The objective of the current section is to verify that the proposed optimal stabilizing filters converge to super-accuracy and improve stability for practical simulations of turbulent flows. To demonstrate super-accuracy for non-linear problems, modally filtered LES and non-filtered ILES of an isentropic vortex will be compared. Following this, non-filtered ILES of the TGV will be compared with LES using the optimized modal filters.

#### 4.1. Non-linear super-accuracy

Super-accuracy of the optimal modal filtering operators for nonlinear problems is verified using an isentropic vortex advection test case in two dimensions. This case is used due to its simple implementation and known exact analytical solution at all times. The advection of





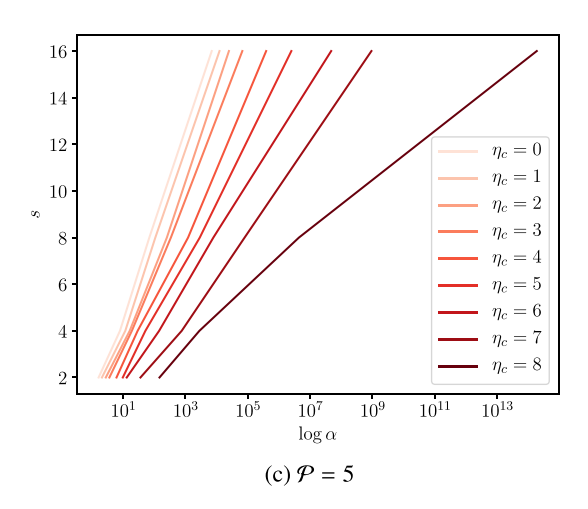
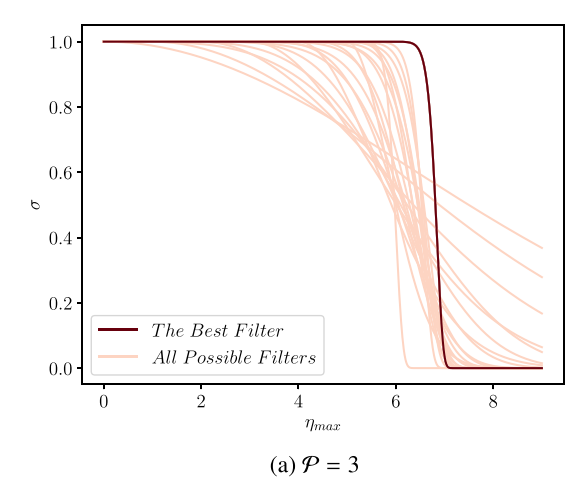


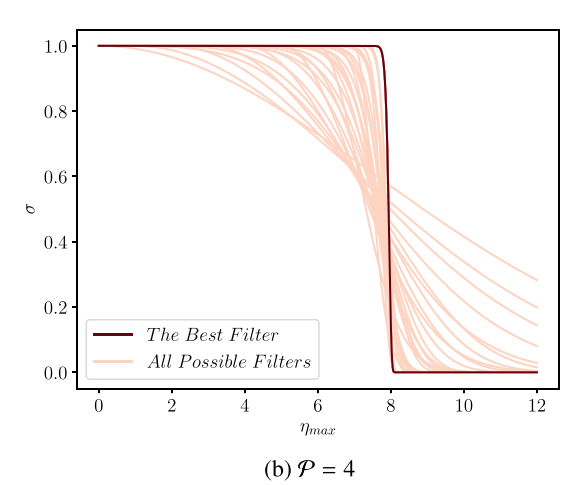
Fig. 7. Plots of stability for different  $\mathcal{P}$ 's at  $\Lambda_{Mach=0.1}$ .

the vortex with the mean flow is simulated using the Euler equations, where the exact entropy remains constant everywhere in the domain. The isentropic vortex has an initial flow field of

$$\rho = \left[1 - \frac{S_v^2 M a^2 (\gamma - 1) e^2 \varphi}{8\pi^2}\right]^{\frac{1}{\gamma - 1}},\tag{38}$$

$$u = \frac{S_v y e^{\varphi}}{2\pi R},\tag{39}$$





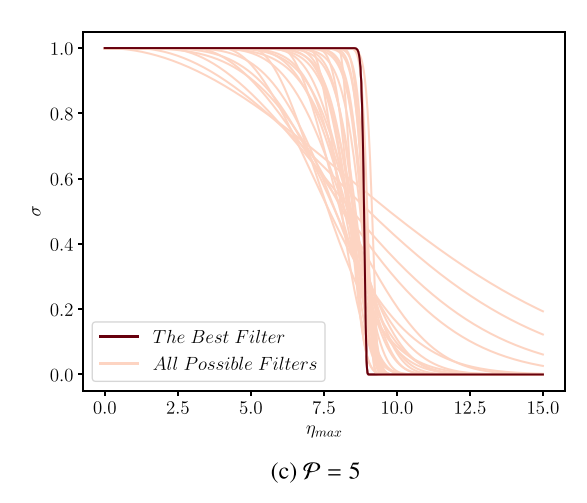


Fig. 8. Plots of all possible filter functions for different  $\mathcal{P}$ 's and the selected ones at  $A_{Mach=0.1}$ .

$$v = 1 - \frac{S_v x e^{\varphi}}{2\pi R},\tag{40}$$

$$P = \frac{\rho'}{\gamma M a^2},\tag{41}$$

where  $\rho$  is the density, u and v are the velocity components, P is the pressure,  $S_v = 13.5$  is the vortex strength, Ma = 0.4 is the free-stream Mach number,  $\gamma = 1.4$  is the heat capacity ratio, R = 1.5 is the radius

Table 1
A summary of order of accuracy for different simulations.

P	Grid size		Order of accuracy		
	Coarse	Fine	Non-filtered	Filtered	
3	40 × 40	60 × 60	7.626557	7.626587	
4	$40 \times 40$	$60 \times 60$	9.104274	9.108797	
5	$20 \times 20$	$40 \times 40$	10.426575	10.633066	

of the vortex, and  $\varphi$  is

$$\varphi = \frac{1 - x^2 - y^2}{2R^2}. (42)$$

The computational domain is a square of length  $[L_x, L_y] = [20, 20]$ , where the centre of vortex is initialized at the coordinate origin. The boundary conditions are specified as periodic in the *y*-direction, and Riemann invariant in the *x*-direction. The modal filters from the three-dimensional configuration are projected onto this 2D basis for quadrilateral elements, and different numbers of elements in the *x* and *y* directions are used. The classical four-stage fourth-order Runge–Kutta scheme is used for time discretization. The simulation is run for a sufficient number of cycles of the vortex through the domain to reach a consistent level of super-accuracy. This corresponded to final simulation times of t = 600, 14000, and 30000 using a time-step size of dt = 0.005, 0.002, and 0.00125 for the  $\mathcal{P} = 3, 4$ , and 5, respectively. The  $L_2$  norm of the density error is computed when the vortex returns to its initial position, and is used to evaluate the accuracy of each filter. The  $L_2$  norm of the error is defined as [52]

$$\|\rho(t)\|^{2} = \sqrt{\int_{-2}^{2} \int_{-2}^{2} (\rho^{\delta}(\mathbf{x}, t) - \rho(\mathbf{x}, t))^{2} d\mathbf{x}},$$
 (43)

where  $\|\rho(t)\|^2$  is the  $L_2$  norm of the density error as a function of time,  $\rho^\delta(\mathbf{x},t)$  is the numerical solution, and  $\rho(\mathbf{x},t)$  is the analytical solution. The solution and flux points are located at tensor products of Gauss points, and an approximate Rusanov Riemann solver, is used. The Rusanov type Riemann solver, used in this study, introduces the inviscid numerical interface flux as

$$F^{inv} = \frac{\hat{\mathbf{n}}_L}{2} \cdot \left( f_L^{inv} + f_R^{inv} \right) + \frac{s}{2} \left( u_L + u_R \right), \tag{44}$$

where  $\hat{\mathbf{n}}_L$  is the normal vector associated with the face,  $f_L^{inv}$  and  $f_R^{inv}$  are the inviscid fluxes at the left and right interfaces, respectively, and  $u_L$  and  $u_R$  are the two discontinuous solution states at an interface. An estimate of the maximum wave speed, s, is

$$s = \sqrt{\frac{\gamma \left(P_L + P_R\right)}{\rho_L + \rho_R}} + \frac{1}{2} |\hat{\boldsymbol{n}}_L \cdot (\boldsymbol{v}_L + \boldsymbol{v}_R)|. \tag{45}$$

A summary of the orders of accuracy for the filtered and non-filtered simulations of different solution polynomial degrees are provided in Table 1, illustrating that the order of accuracy of the filtered simulation is almost identical to that of the non-filtered simulation, and both converge with super-accuracy.

#### 4.2. The Taylor-Green Vortex

In order to study the suitability of the proposed filters for LES, the Navier–Stokes equations are solved using the TGV case. Several authors have analysed the TGV using discontinuous high-order methods. The TGV has been studied using FR [53,54], modal DG [55,56], recovery-based DG method [57], DG Spectral Element method [58–60], and is studied in this paper using the FR approach.

The rate of kinetic energy dissipation along with enstrophy are computed to validate the accuracy of the optimal filtering functions. The temporal evolution of total kinetic energy integrated over the domain is

$$E_k = \frac{1}{\rho_0 \Omega} \int_{\Omega} \rho \frac{\mathbf{V} \cdot \mathbf{V}}{2} d\Omega, \tag{46}$$

where  $E_k$  is the total kinetic energy,  $\varOmega$  is the volume of the domain,  $\rho$  is the density, and V is the velocity vector. The energy-based dissipation rate is then defined as

$$\epsilon(E_k) = -\frac{dE_k}{dt}.\tag{47}$$

The temporal evolution of enstrophy is

$$\varepsilon = \frac{1}{\rho_0 \Omega} \int_{\Omega} \rho \frac{\boldsymbol{\omega} \cdot \boldsymbol{\omega}}{2} d\Omega, \tag{48}$$

where  $\boldsymbol{\omega}$  is the vorticity. And the vorticity-based dissipation rate is [61]

$$\epsilon(\epsilon) = \frac{2\mu}{\rho}\epsilon. \tag{49}$$

In the incompressible limit, the difference between the physical dissipation,  $\epsilon(\varepsilon)$ , and the observed dissipation,  $\epsilon(E_k)$ , is due to numerical dissipation.

The vortices are initialized at Re = 1600 based on the length scale L and velocity scale  $U_0$ , and the Mach number of Ma = 0.1. The domain is a periodic cube of dimensions  $0 \le x, y, z \le 2\pi L$ , with nominally  $64^3$  total number of DoF. Each simulation is run with  $\mathcal{P} =$ 3,4, and 5 using different strengths of the filtering function optimized for Ma = 0.1, 0.2, 0.3, 0.4, and 0.5 along with a non-filtered simulation. The results are compared to the reference DNS of Van Rees [61] with an extended time history provided through the high-order workshop [29]. The solution and flux points are located at tensor products of Gauss points, and the Rusanov and second method of Bassi and Rebay (BR2) are used for the common inviscid and viscous flux. Plots of the kinetic energy evolution in time, the rate of  $E_{k}$  dissipation based on both  $E_{k}$ , and  $\varepsilon$  for different solution polynomial degrees of  $\mathcal{P} = 3, 4$ , and 5 using different filtering functions are given in Figs. 9-11. The kinetic energy spectrum of high wavenumbers with different strengths of the filtering operator along with the non-filtered simulation are computed utilizing a spectral code by Navah [62], and is shown in Fig. 12. Also isosurfaces of Q-criterion for the TGV at  $20T_{char}$  for different solution polynomial degrees are shown, with and without the filtering operator, in Fig. 13.

In Fig. 9, it can be seen that the dissipation of  $E_k$  is slightly higher for the filtered simulation, and the  $E_k$  is always less than the DNS results except for  $\mathcal{P}=3$ . The higher dissipation of a filtered solution is expected, since the filtering operator is removing high wavenumber components of the flow field. The energy-based rate of  $E_k$  dissipation is shown in Fig. 10. In general, the filtered simulations are slightly more dissipative than the non-filtered simulation, an effect that increases with filter strength. Since more energy is dissipated earlier on in the filtered simulations, this trend reverses in the later time periods.

Fig. 11 shows that the enstrophy-based  $E_k$  dissipation is slightly under-predicted in the filtered simulations. Based on Eq. (48), the small scale structures are enstrophy dominated structures in the turbulent flow, which are filtered when the filtering operator is active. Hence, the lower enstrophy observed in the filtered simulations. Since the filtering operator dissipates the energy of the higher modes, we expect there will be less energy in high wavenumbers for filtered simulations. This is depicted in Fig. 12, where the kinetic energy spectrum of high wavenumbers is given at  $20T_{char}$ . It can be seen that for stronger filtering operators, there is in fact reduced energy in higher modes, as expected. Finally, from Fig. 13 showing isosurfaces of Q-criterion, it is evident that when the filtering operator is applied, the general scale of the turbulent structures is larger than the non-filtered simulations.

In summary, we observe that the filtering operators tend to slightly increase the amount of numerical dissipation for all polynomial degrees. This is primarily due to damping of high-frequency modes in the solution. Nevertheless, the overall accuracy at each polynomial degree and for all filtering strengths is not impacted significantly.

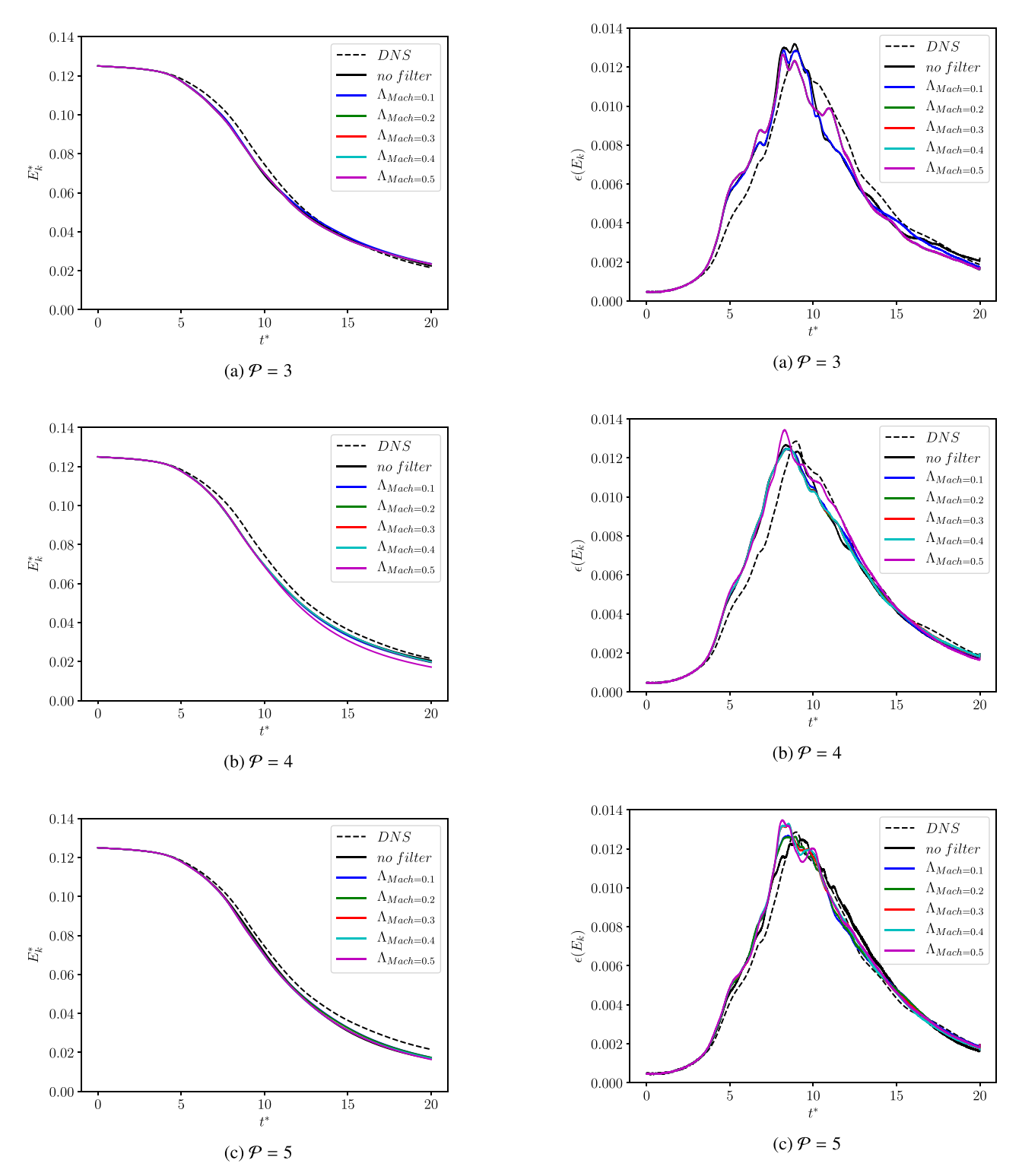
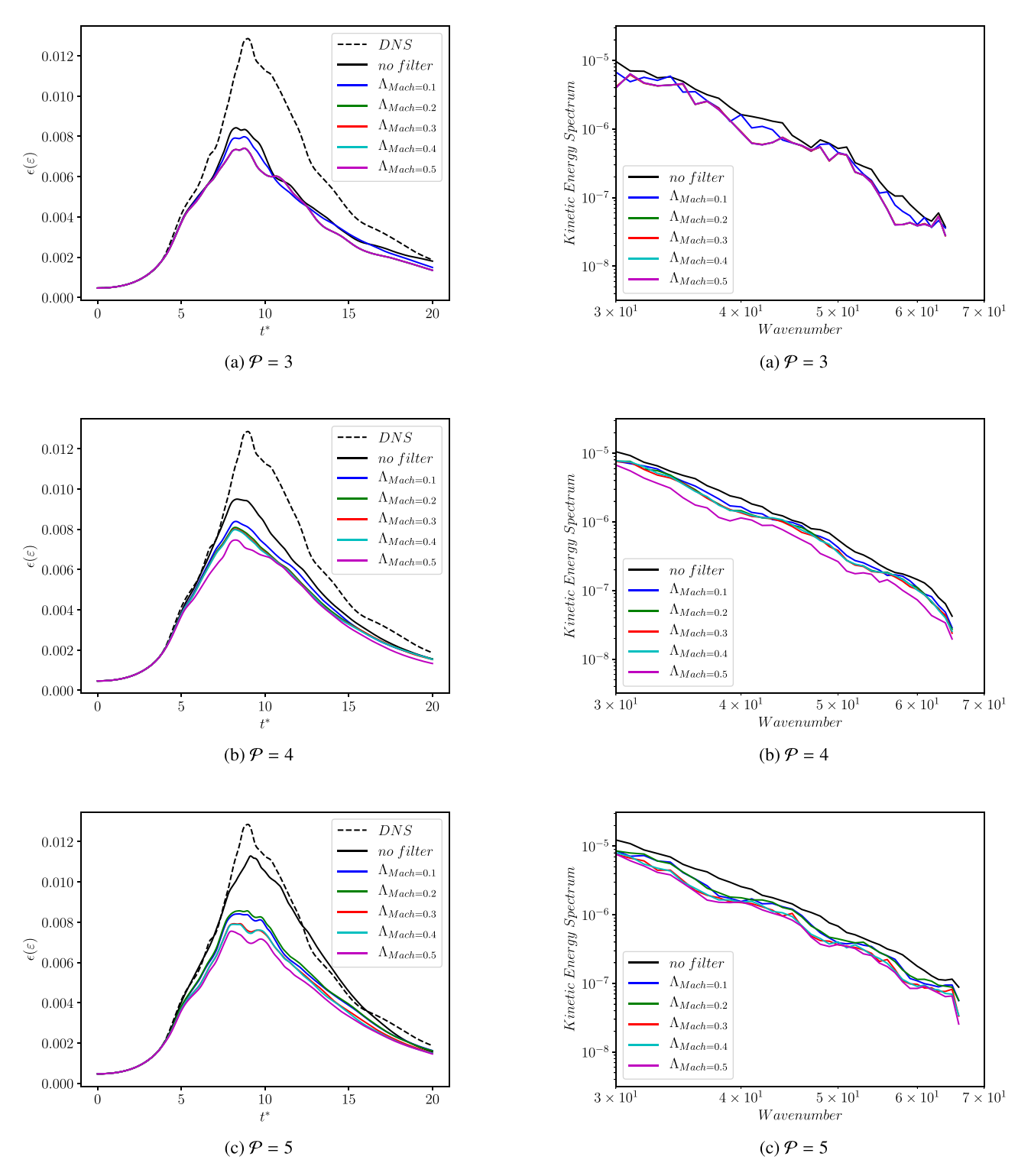


Fig. 9. The evolution of kinetic energy in time for different solution polynomials.

 $\textbf{Fig. 10.} \ \ \textbf{The energy-based rate of kinetic energy dissipation for different solution polynomials.}$ 



 $\begin{tabular}{ll} {\bf Fig.~11.} & {\bf The~enstrophy-based~rate~of~kinetic~energy~dissipation~for~different~solution~polynomials.} \end{tabular}$ 

Fig. 12. The kinetic energy spectrum of high wavenumbers at  $20T_{char}$  for different solution polynomial degrees.

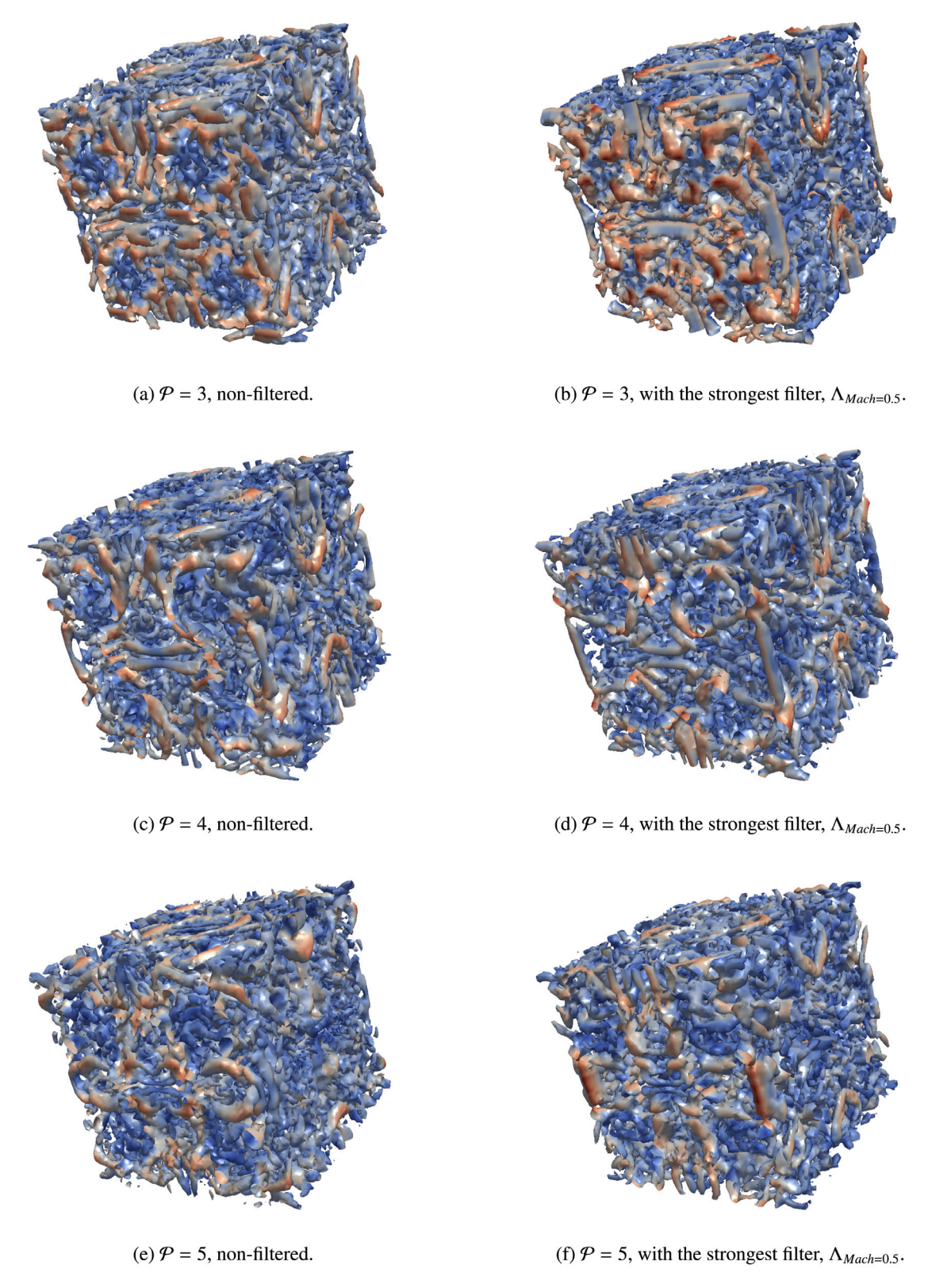


Fig. 13. Isosurfaces of Q-criterion for the TGV at  $20T_{char}$  for different polynomial degrees.

#### 4.3. The Taylor-Green Vortex on a non-linear mesh

Abe et al. [63] and Trojak et al. [64] studied the TGV on a fully non-linear mesh. In this study, the effects of filtering is investigated on non-linear elements. The case setup is the same as the previous section; however, the solution points are perturbed using the following equations [64]

$$x' = x + \frac{l}{n_x} A \sin\left(\frac{k_g \pi y}{l}\right) \sin\left(\frac{k_g \pi z}{l}\right),\tag{50}$$

$$y' = y + \frac{l}{n_y} A \sin\left(\frac{k_g \pi x}{l}\right) \sin\left(\frac{k_g \pi z}{l}\right),\tag{51}$$

$$z' = z + \frac{l}{n_z} A \sin\left(\frac{k_g \pi x}{l}\right) \sin\left(\frac{k_g \pi y}{l}\right),\tag{52}$$

where  $k_g$  is the grid wavenumber and A is the grid wave amplitude, and in keeping with Abe et al. [63] and Trojak et al. [64] we will use  $k_g=4$  and A=0.4. l is the length of the computational domain and is equal to  $2\pi$ , and  $n_i$  is the number of elements in the i-direction. Fig. 14 shows a sub-sample of the non-linear mesh.

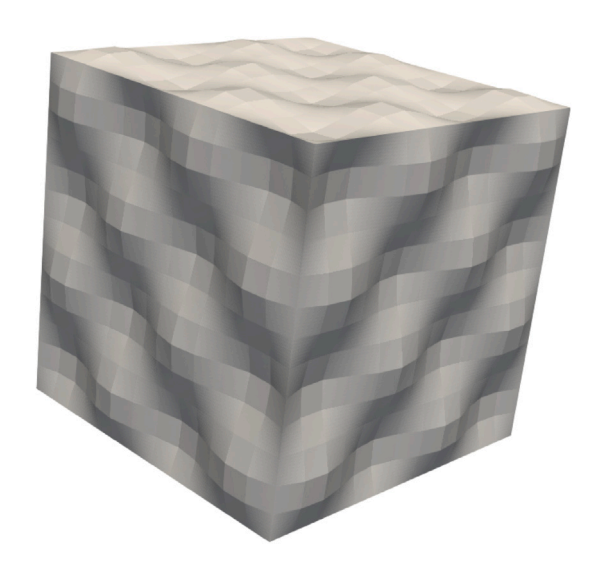
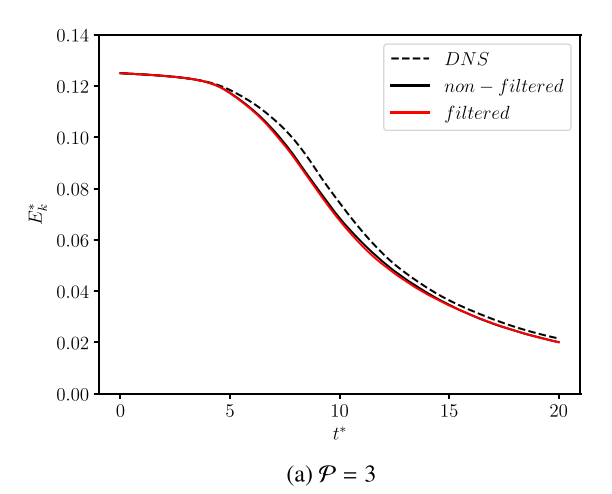


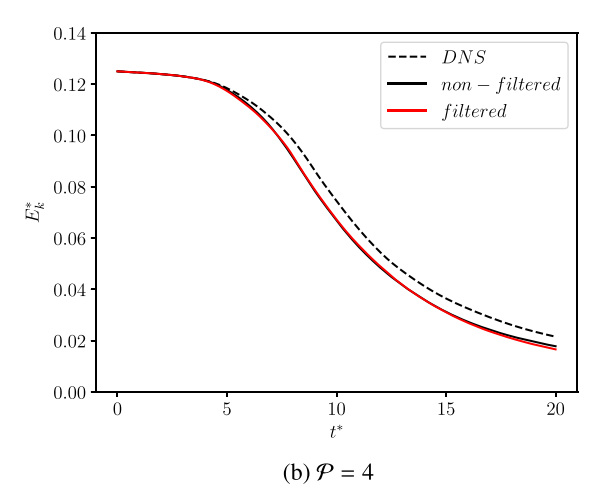
Fig. 14. A sub-sample of the computational domain.

The evolution of kinetic energy in time, the energy and enstrophybased rate of kinetic energy dissipation, and the kinetic energy spectrum of high wavenumbers are obtained similar to the previous section, and are shown in Figs. 15, 16, 17, and 18, respectively. The results of this section is similar to the TGV using a linear mesh, which shows that the filtering operator can also be applied with fully non-linear meshes.

# 5. Numerical examples

In this section, a previously unstable turbulent channel test case, along with an airfoil at a high angle of attack are studied. The objective is to explore the stabilization properties of the proposed filters and their accuracy for a set of benchmark problems. In this section, the strongest filtering operator,  $\Lambda_{Mach=0.5}$ , is used. The rationale behind this choice is that the strongest filter would be expected to have the most significant impact on the results.





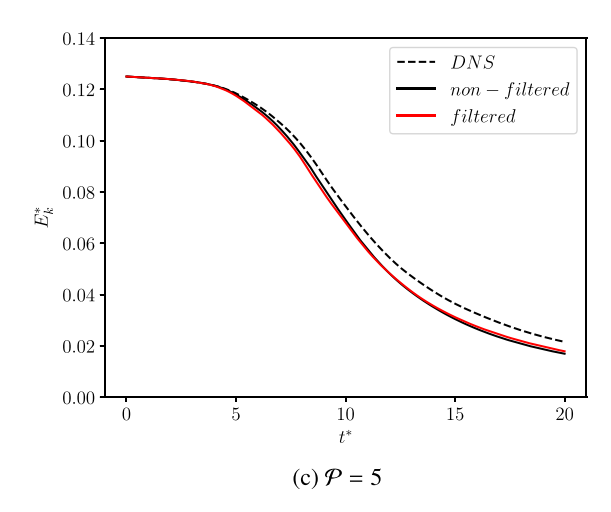
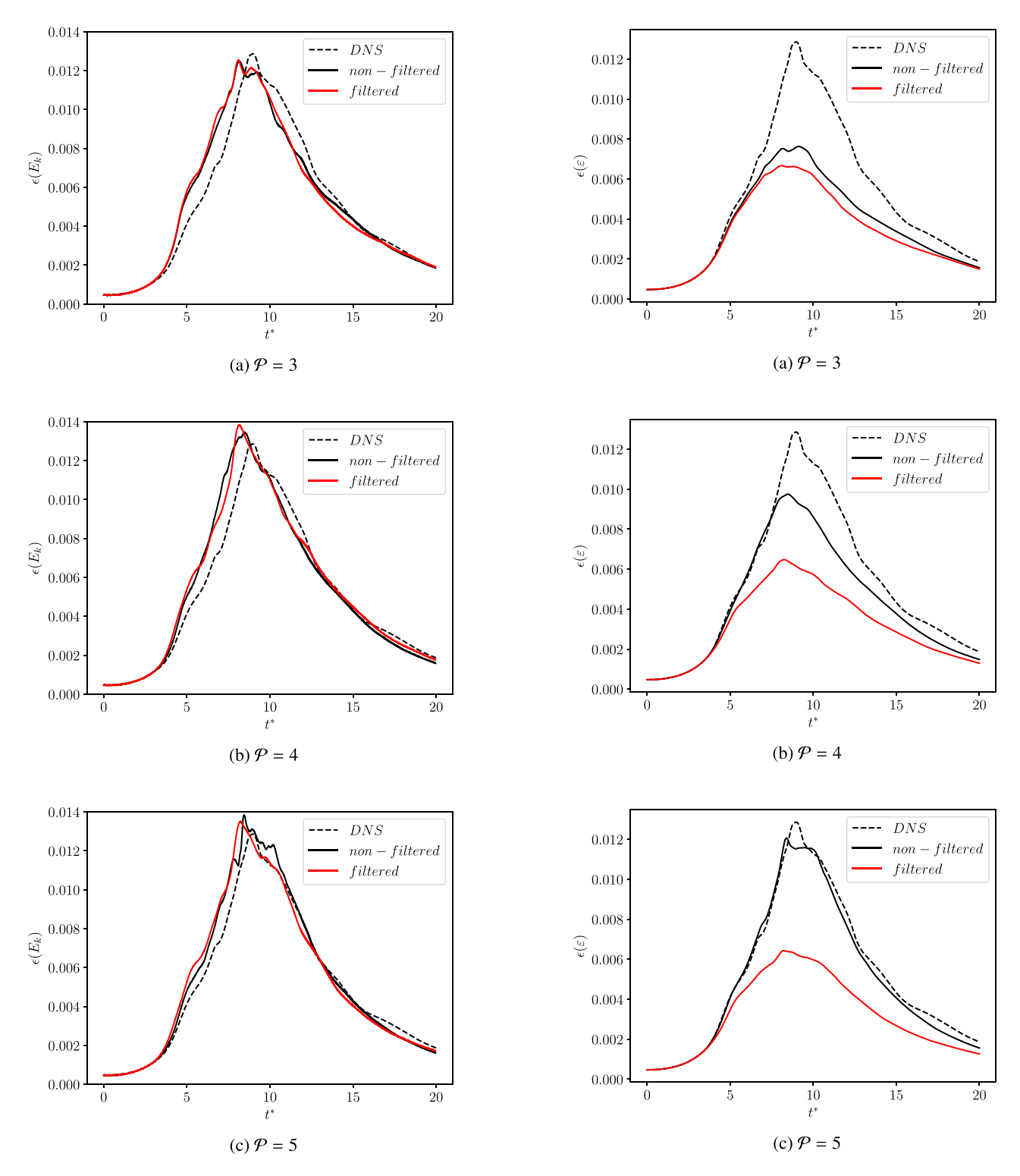
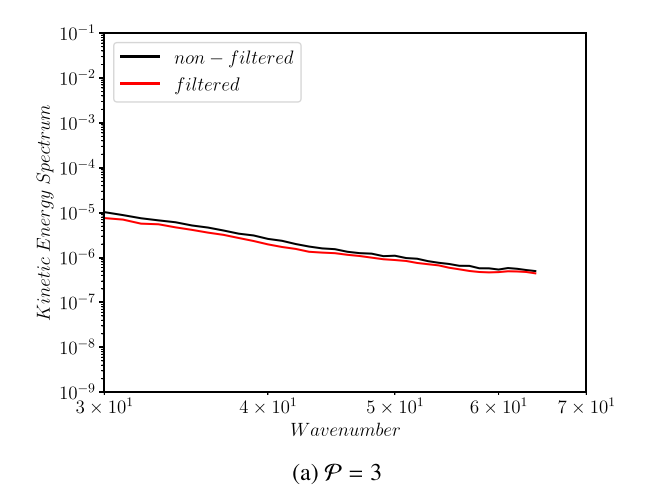


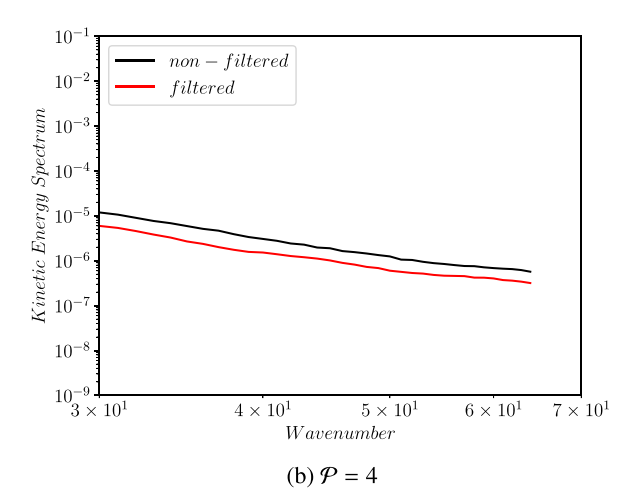
Fig. 15. The evolution of kinetic energy in time for different solution polynomials, for the fully non-linear mesh.



 $\begin{tabular}{ll} {\bf Fig.~16.} & The energy-based rate of kinetic energy dissipation for different solution polynomials, for the fully non-linear mesh. \end{tabular}$ 

Fig. 17. The enstrophy-based rate of kinetic energy dissipation for different solution polynomials, for the fully non-linear mesh.





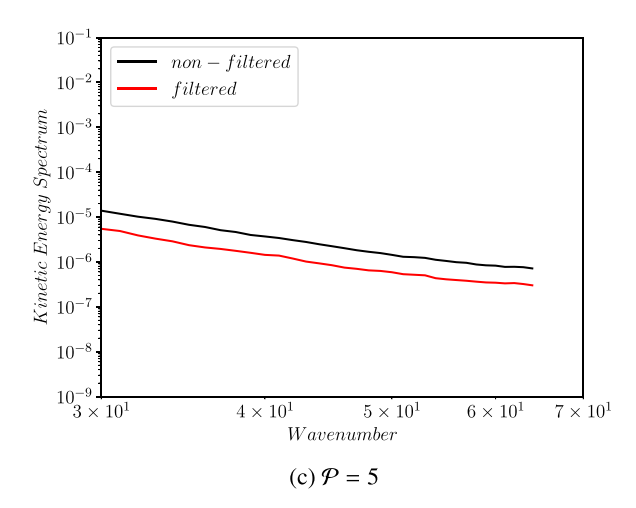


Fig. 18. The kinetic energy spectrum of high wavenumbers at  $20T_{char}$  for different solution polynomial degrees, for the fully non-linear mesh.

#### 5.1. Turbulent channel

Fully-developed turbulent channel flow is studied as validation for wall-bounded turbulent flows, due to its simple geometry and boundary conditions. The fully-developed assumption means that all statistical properties of the flow are independent of time. In turbulent channel studies, it is conventional to use the friction velocity defined as

$$u_{\tau} = \sqrt{\frac{\tau_w}{\rho}},\tag{53}$$

where  $\tau_w$  is the wall shear stress.

Kim, Moin and Moser [65] originally performed DNS of turbulent channel flow. In the present research, ILES and LES, using the proposed optimized modal filter, are performed and compared to this DNS result. The domain is of size  $[L_x, L_y, L_z] = [2\pi\delta, 2\delta, \pi\delta]$  with periodic boundary conditions in the streamwise (x) and spanwise (z) directions and a noslip boundary condition is applied at the walls, where  $\delta=1$  is the channel half-width. The initial conditions are Mach number of Ma=0.3 and bulk velocity Reynolds number of  $Re_b=6800$  based on the channel half-width. A mean pressure gradient is added such that the friction velocity Reynolds number will converge to  $Re_\tau=395$ . The grid points in the y-direction are computed using the following hyperbolic function [66]

$$y_j = \frac{1}{2\alpha} \tanh\left[\left(-1 + \frac{2j}{DoF_y}\right) \tanh^{-1}\alpha\right] + 0.5,\tag{54}$$

where  $\alpha=0.96$  is the stretching factor and  $DoF_y$  is the number of solution points in the y direction. The present simulations are summarized in Table 2.

In this study, we used 3/8 of the total number of DoF required for DNS in all directions to simulate the turbulent channel with polynomial degrees of  $\mathcal{P}=3,4$ , and 5. This simulation is stable for  $\mathcal{P}=3$  and 4, so it is run with and without the filtering to compare filtered simulations with non-filtered ones. The filtering operator is applied for the simulation with  $\mathcal{P}=5$  to stabilize it. The strongest filtering operator,  $\Lambda_{Mach=0.5}$ , is used for all filtered simulations.

Velocity Power Spectral Density (PSD) for each simulation are given in Figs. 20–22 for different non-dimensional distances from the wall, shown in Fig. 19. The mean velocity, Reynolds stresses, and root-mean-squared velocity fluctuations are then given in Figs. 23, 24, and 25, respectively, for different polynomial degrees. Finally, isosurfaces of Q-criterion are shown in Fig. 26 for all simulations.

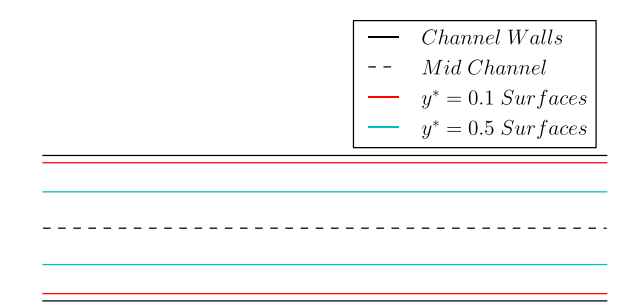


Fig. 19. The surfaces used for velocity PSD computation.

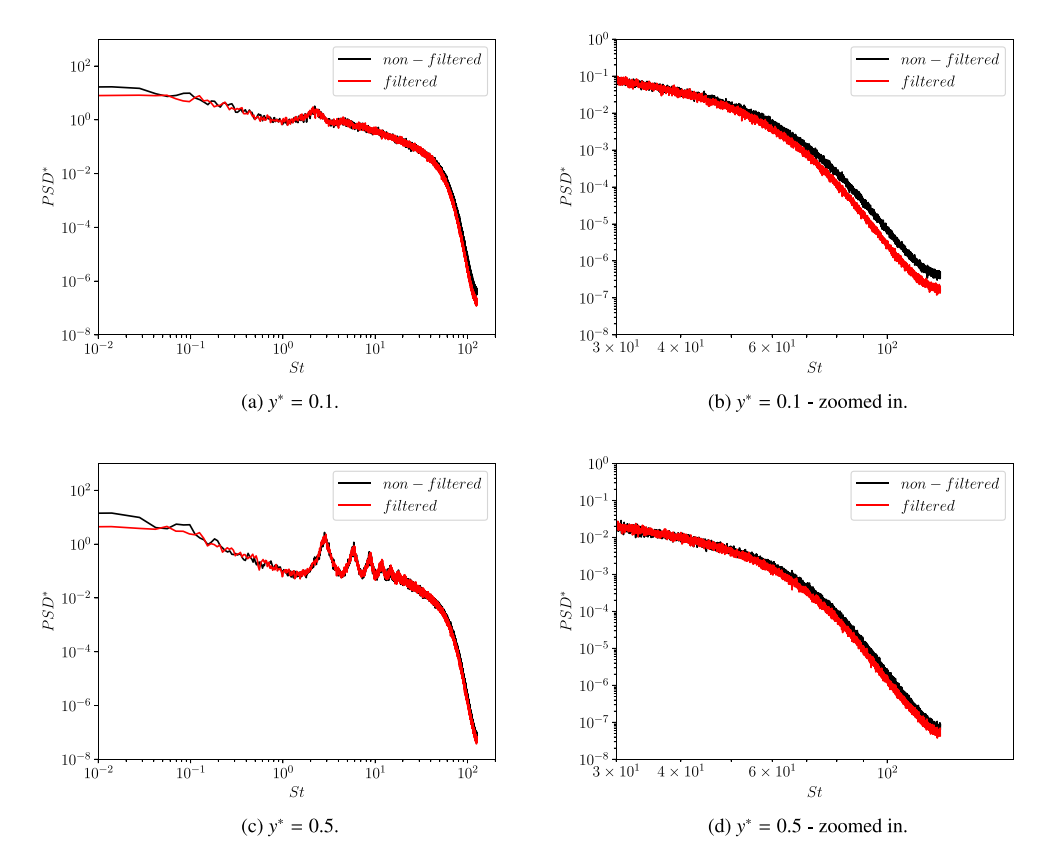


Fig. 20. The velocity power spectral density at different locations for  $\mathcal{P}=3$ .

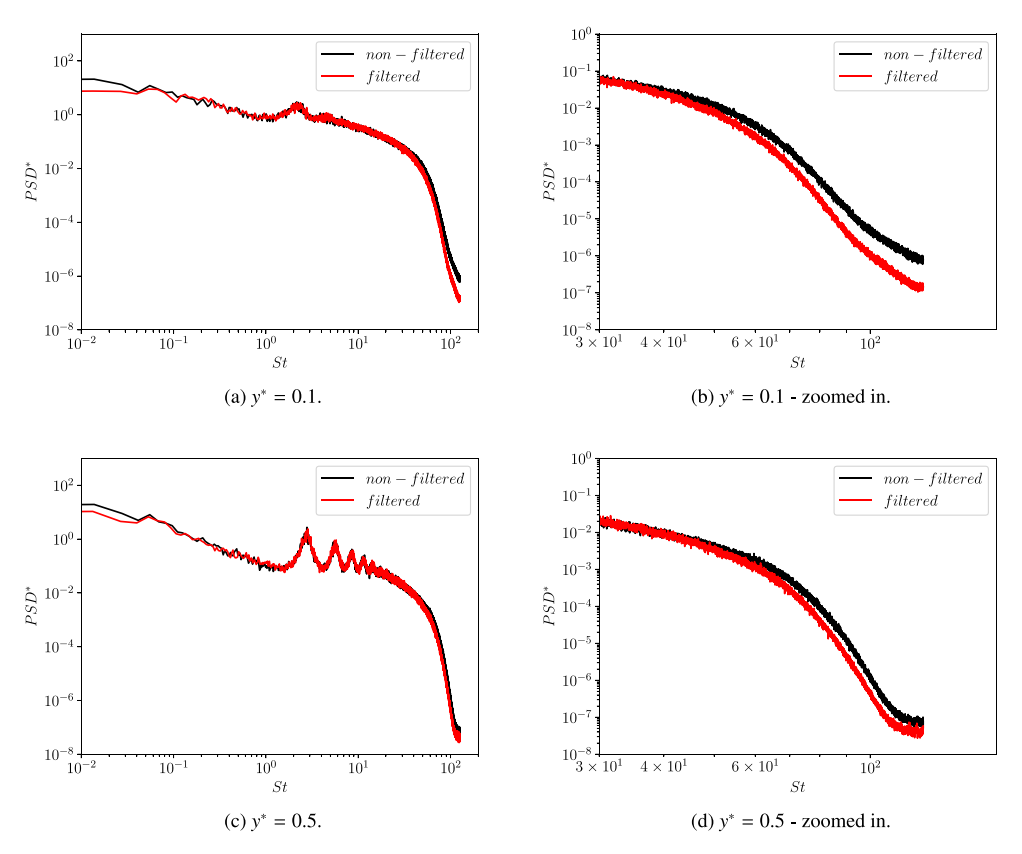


Fig. 21. The velocity power spectral density at different locations for  $\mathcal{P}=4$ .

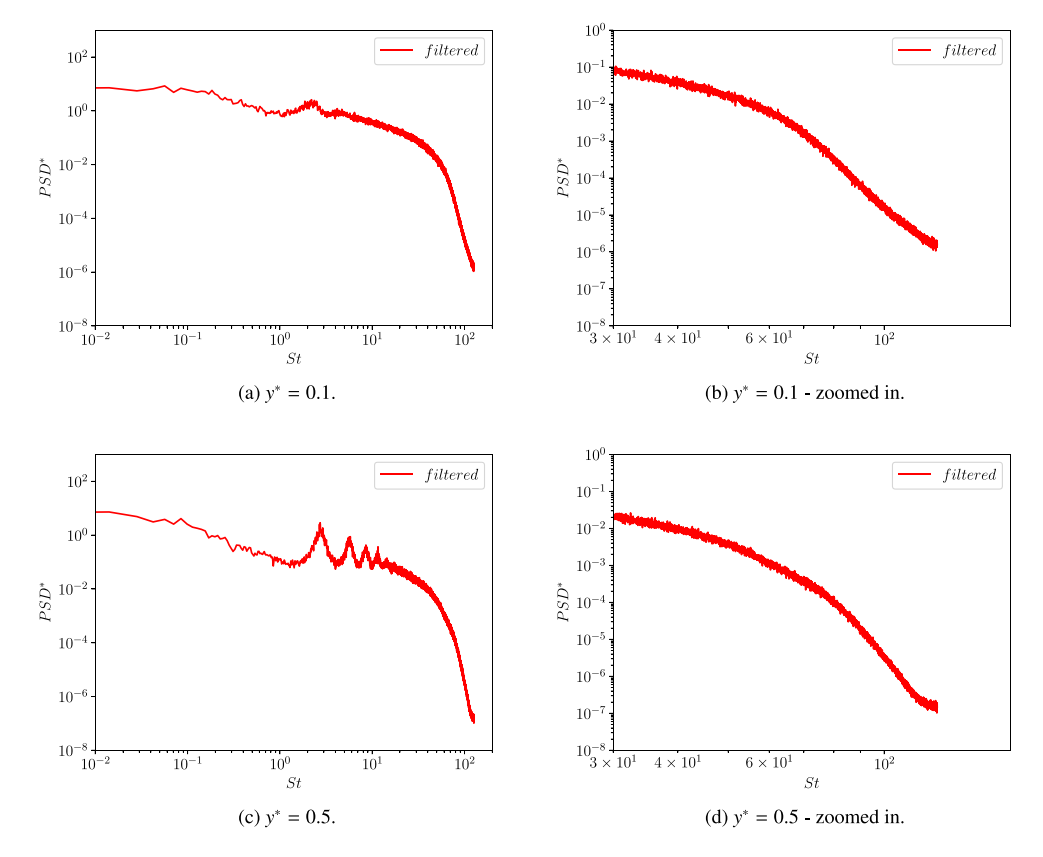


Fig. 22. The velocity power spectral density at different locations for P = 5.

**Table 2** Parameters of the simulations where  $N_{ei}$  is the number of elements in *i*th-direction and  $\Delta i^+$  is the distance of the first grid point off the boundary in *i*th-direction non-dimensionalized by  $u_{\tau}$  and the kinematic viscosity, v.

$\mathcal{P}$	Filter	$Re_{\tau}$	$\frac{L_x}{\delta}$	$\frac{L_y}{\delta}$	$\frac{L_z}{\delta}$	$T_f$	$\Delta x^+$	$\Delta y^+$	$\Delta z^+$	$N_{ex}$	$N_{ey}$	$N_{ez}$	DoF
3	off	395	$2\pi$	2	π	170	25.85	0.92	17.23	24	18	18	497664
3	on	395	$2\pi$	2	$\pi$	170	25.85	0.92	17.23	24	18	18	497664
4	off	395	$2\pi$	2	$\pi$	170	24.82	0.88	16.55	20	15	15	562500
4	on	395	$2\pi$	2	$\pi$	170	24.82	0.88	16.55	20	15	15	562500
5	on	395	$2\pi$	2	$\pi$	170	25.85	0.92	17.23	16	12	12	497664

From the velocity power spectral density plots for  $\mathcal{P}=3$  and 4, shown in Figs. 20 and 21, it can be seen that for the filtered simulations, only the higher modes have reduced power relative to the non-filtered simulations, which shows that filtering only affects the higher modes, as by design. Fig. 22, shows the velocity power spectral density for  $\mathcal{P}=5$  at different locations, in which less energy is observed at high wavenumbers, compared to low wavenumbers. In Figs. 23(a) and 23(b), we can see excellent agreement between the mean velocity profile of the filtered and non-filtered simulations for  $\mathcal{P}=3$  and 4. Similar behaviour is observed in Fig. 23(c) between the filtered simulation and the DNS results for  $\mathcal{P}=5$ .

The Reynolds stresses shown in Figs. 24 and 25 also show good agreement between the ILES/LES results and the DNS. The use of filtering has negligible effect on the results, and no loss in accuracy is seen for filtered simulations. Importantly, even more accurate results are obtained with filtering in the near wall region compared to the non-filtered simulation for  $\mathcal{P}=3$ , as shown in Fig. 25(a), for  $10 < y^+ < 40$ . The maximum streamwise velocity fluctuation occurs at  $y^+ \approx 12$  for both filtered and non-filtered simulations, consistent with the DNS, as observed in Fig. 25. Finally, isosurfaces of Q-criterion are shown in

Fig. 26, where it can be seen that by applying the filtering operator, the turbulent structures are qualitatively larger than the non-filtered simulation for  $\mathcal{P}=3$  and 4.

In summary, we find that the filtering operators were suitable for LES of turbulent channel flow. They stabilized an otherwise unstable simulation, and produced results consistent with the reference DNS data. Also, in the case of  $\mathcal{P}=3$ , the filter produced slightly more accurate results, even though it was not required for stability.

# 5.2. Airfoil

Flow over a NACA0020 airfoil at an angle of attack of  $\alpha=20$ , Mach number of Ma=0.2, and Re=20000 is simulated both without filtering and with the strongest filter operator,  $\Lambda_{Mach=0.5}$ . A second order P-ERK scheme is used for marching in time [67]. The mesh used for this simulation is shown in Fig. 27, which consists of 68590 hexahedral elements. The domain has a periodic span of 0.45c, which is sufficient for span-wise decorrelation [68]. Furthermore, the first solution point off the wall is located at  $y^+\approx 0.7$ , within the viscous sublayer. Each simulation is started with  $\mathcal{P}=1$ , and then restarted at  $\mathcal{P}=3$  and run

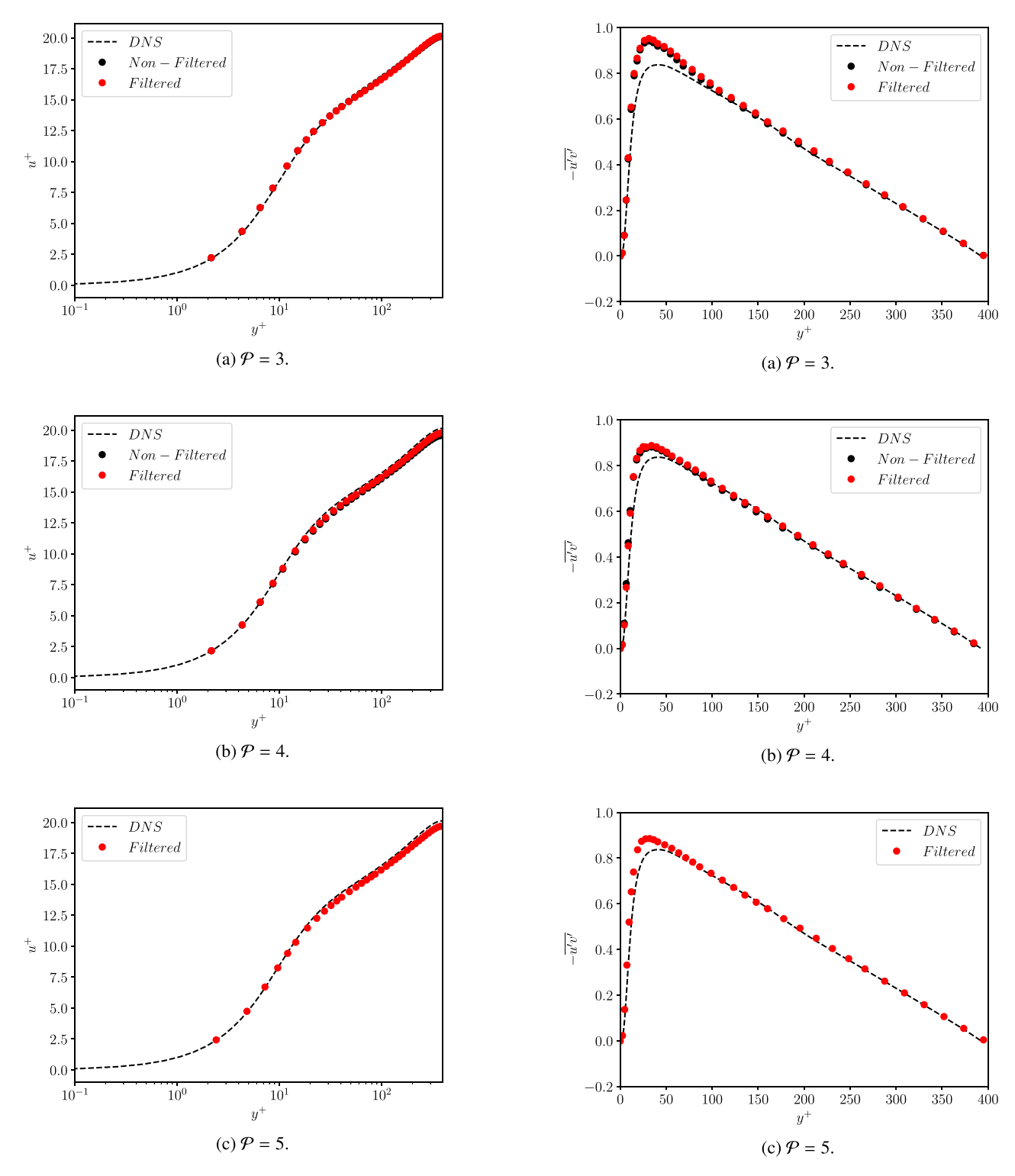


Fig. 23. Mean velocity profile for different solution polynomial degrees.

 $Fig.\ 24.\ \ Reynolds\ shear\ stresses\ for\ different\ solution\ polynomial\ degrees.$ 

**Table 3**Comparison between the non-filtered, filtered, and DNS results.

1		
Simulation	$\overline{C_L}$	$\overline{C_D}$
DNS [68]	0.64	0.35
Non-filtered ILES	0.639	0.353
Modally-filtered LES	0.651	0.357

for 100 convective times. Statistical averages are computed over the final 80 convective times.

Isosurfaces of Q-criterion coloured by velocity magnitude are shown in Fig. 28. Qualitatively, the large scale structures show similar behaviour, while spurious small scale structures appear to be damped in the filtered simulation.

Time-averaged values,  $\overline{C_L}$  and  $\overline{C_D}$  (see Fig. 29), are compared to DNS results in Table 3, which shows excellent agreement between the DNS and both filtered LES and non-filtered ILES results. The time-averaged pressure coefficient for both the filtered and non-filtered simulations are shown in Fig. 30, where the results are nearly identical. In conclusion, applying the optimized filtering operator does not significantly degrade solution accuracy, and the results are in excellent agreement with the non-filtered simulation and reference DNS data.

#### 6. Conclusions

In this study a new filtering operator was proposed for stabilization of high-order LES. This operator is novel in the sense that its strength is made independent of the time-step size. Moreover, all of the filtering operators are optimized to yield the minimum filter strength for stabilization, and preserve the order of accuracy for solution polynomial of degrees P = 3,4, and 5 while maintaining stability in the limit of an infinite Reynolds number TGV. Numerical results show that the proposed filter stabilizes otherwise unstable simulations, while maintaining good agreement with non-filtered stable solutions. Hence, these filtering functions are an appealing stabilization technique for highorder spatial discretizations. Future work will focus on their application to higher-Reynolds number LES to determine the range of applications for which they can provide effective stabilization. It is well-known that another important factor for the stability of the FR approach is the choice of a correction function [24], and an interesting area of future work would be to explore optimizing filters for different correction functions, and even different high-order numerical schemes such as SD and/or DG.

#### Data statement

Data relating to the results in this manuscript can be downloaded from the publication's website under a CC-BY-NC-ND 4.0 license.

#### CRediT authorship contribution statement

**Mohsen Hamedi:** Software, Validation, Formal analysis, Investigation, Data curation, Writing – original draft, Visualization. **Brian C. Vermeire:** Conceptualization, Methodology, Software, Resources, Writing – review & editing, Supervision, Project administration, Funding acquisition.

## Declaration of competing interest

The authors declare that they have no known competing financial interests or personal relationships that could have appeared to influence the work reported in this paper.

Table 4 The optimum filter function parameters of different strengths for P = 3.

P = 3		
$\Lambda_{Mach=0.1}$	$\eta_c$ s $\alpha$	5 16 217075.2759552002
$\Lambda_{Mach=0.2}$	$ \eta_c $ $s$ $ \alpha$	5 16 1202391046.135873
$\Lambda_{Mach=0.3}$	$\eta_c$ $s$ $\alpha$	5 16 917162317.9408722
$\Lambda_{Mach=0.4}$	$ \eta_c $ $s$ $\alpha$	5 16 1392939017.611743
$\Lambda_{Mach=0.5}$	$\eta_c$ $s$ $\alpha$	5 16 1457812117.278677

 $\begin{tabular}{ll} \textbf{Table 5} \\ \textbf{The optimum filter function parameters of different strengths for } \mathcal{P}=4. \\ \end{tabular}$ 

P = 4		
	$\eta_c$	7
$\Lambda_{Mach=0.1}$	S	16
	α	291498213413.2662
	$\eta_c$	7
$\Lambda_{Mach=0.2}$	S	16
	α	1665739102108.521
	$\eta_c$	7
$\Lambda_{Mach=0.3}$	S	16
	α	2314754521287.192
	$\eta_c$	7
$\Lambda_{Mach=0.4}$	S	16
	α	2668366061332.971
	$\eta_c$	6
$\Lambda_{Mach=0.5}$	S	16
	α	15565248612801.27

# Acknowledgements

The authors acknowledge support from the Natural Sciences and Engineering Research Council of Canada (NSERC), [RGPAS-2017-507988, RGPIN-2017-06773]. This research was enabled in part by support provided by Calcul Quebec (www.calculquebec.ca), SciNet (www.scinethpc.ca), and Compute Canada (www.computecanada.ca) via a Resources for Research Groups allocation. M.H acknowledges support from a Hydro Québec Graduate Award. Also, the authors acknowledge Dr. Farshad Navah for providing his script to compute the Taylor–Green spectra.

# Appendix A. The stability threshold for different strengths of the filtering

See Figs. 31-34.

Appendix B. All of the possible filtering functions and the best one

See Figs. 35-38.

Appendix C. The optimum parameters for the filter function

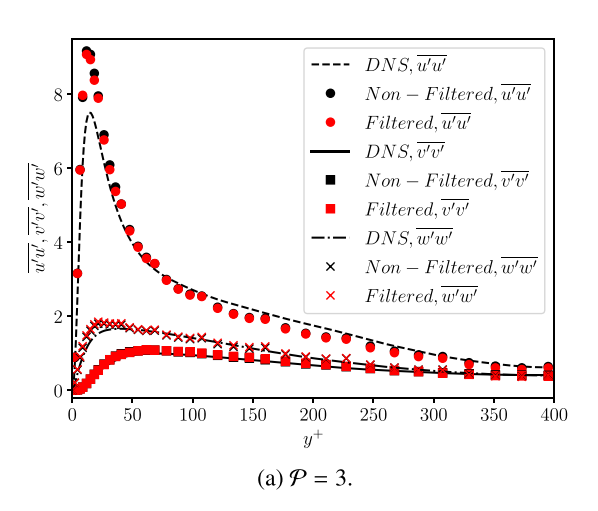
See Tables 4-6.

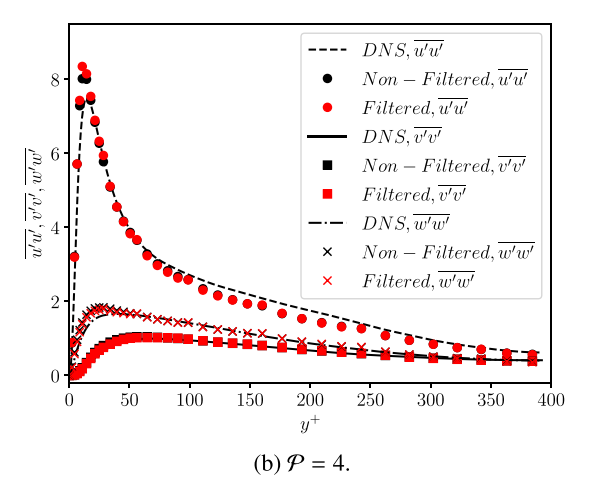
#### Appendix D. Supplementary data

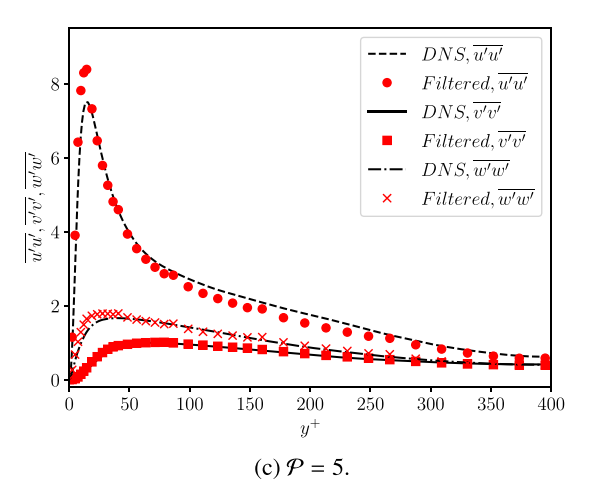
Supplementary material related to this article can be found online at https://doi.org/10.1016/j.compfluid.2021.105301.

 $\label{eq:table 6} \textbf{The optimum filter function parameters of different strengths for } \mathcal{P} = 5.$ 

P = 5		
	$\eta_c$	8
$\Lambda_{Mach=0.1}$	S	16
	α	187367342908422.5
	$\eta_c$	8
$\Lambda_{Mach=0.2}$	S	16
	α	86245118555321.83
	$\eta_c$	6
$\Lambda_{Mach=0.3}$	S	16
	α	18566388095.02125
	$\eta_c$	6
$\Lambda_{Mach=0.4}$	S	16
	α	48469598837.49486
	$\eta_c$	6
$\Lambda_{Mach=0.5}$	S	16
	α	321516181278.2288







 $\textbf{Fig. 25.} \ \ Root\text{-}mean\text{-}squared \ \ velocity \ \ fluctuations \ \ for \ \ different \ \ solution \ \ polynomial \ degrees.$ 

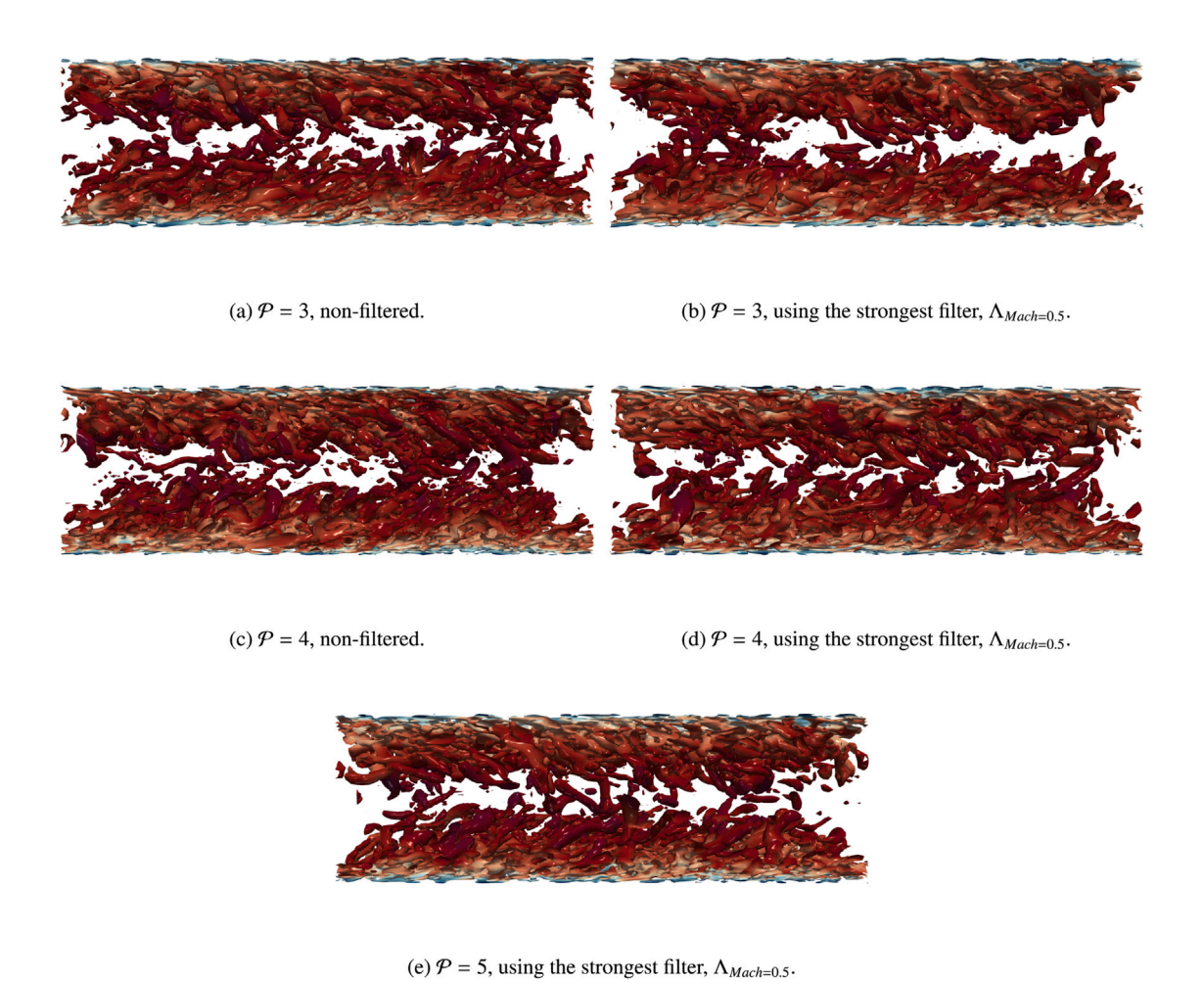
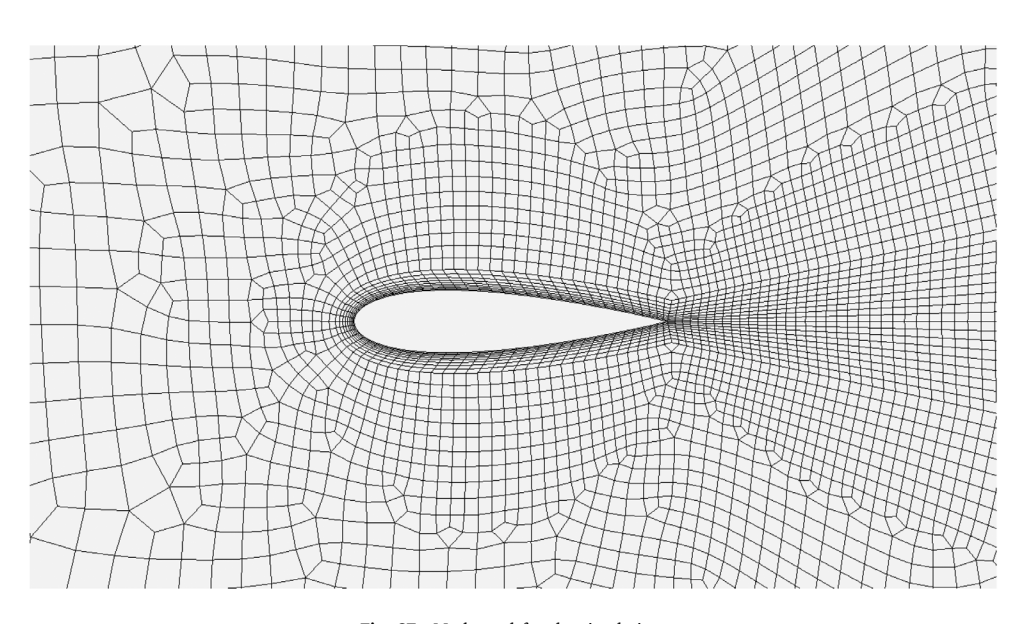
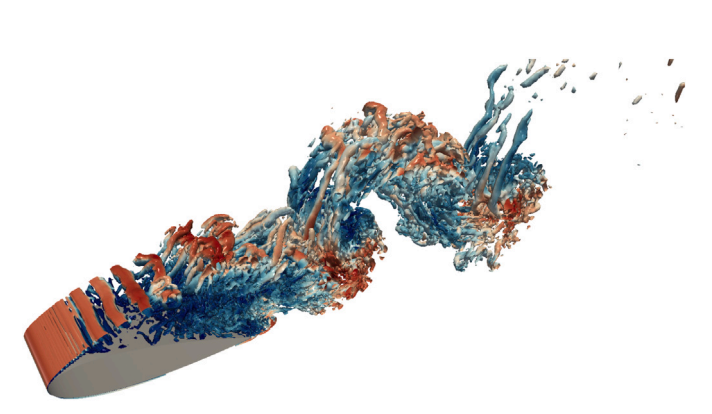
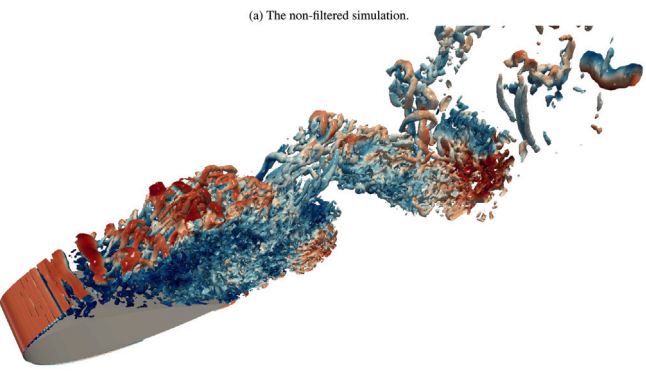


Fig. 26. Isosurfaces of Q-criterion, coloured by velocity, for all of the simulations.



 $\label{eq:Fig.27.} \textbf{Mesh used for the simulation}.$ 





(b) The filtered simulation.  ${\bf Fig.~28.~ The~isosurfaces~of~Q-criterion~after~200} T_{char}.$ 

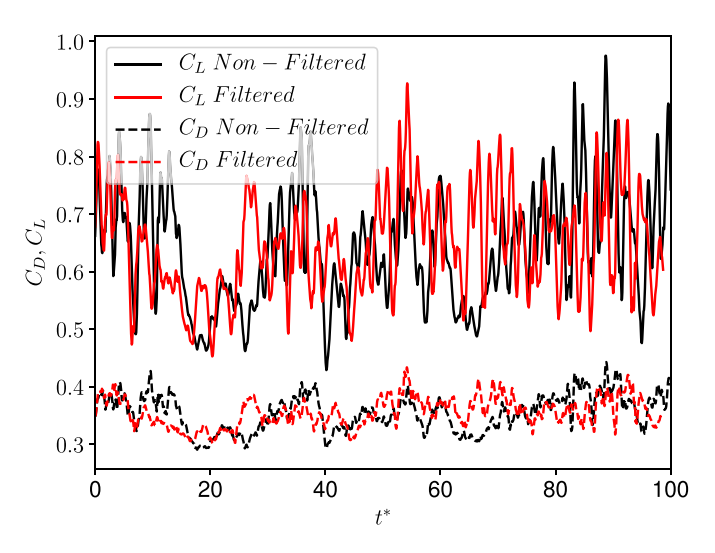


Fig. 29. The lift and drag coefficients evolution in time.

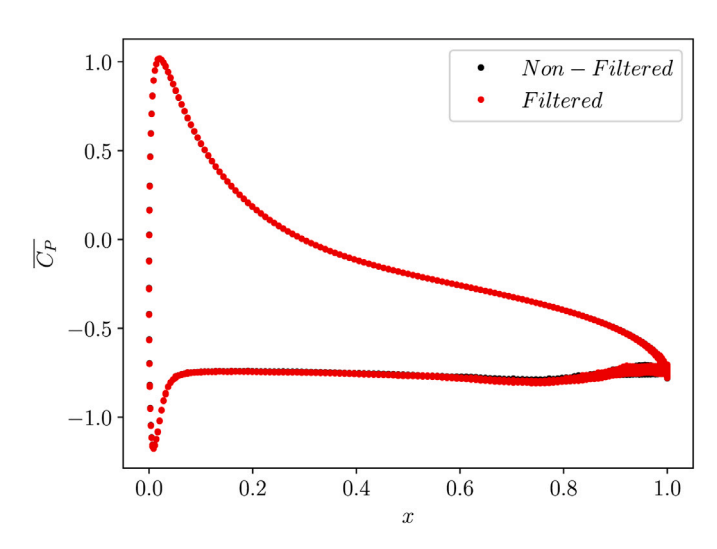


Fig. 30. The time-averaged pressure coefficient on the surface of the airfoil.

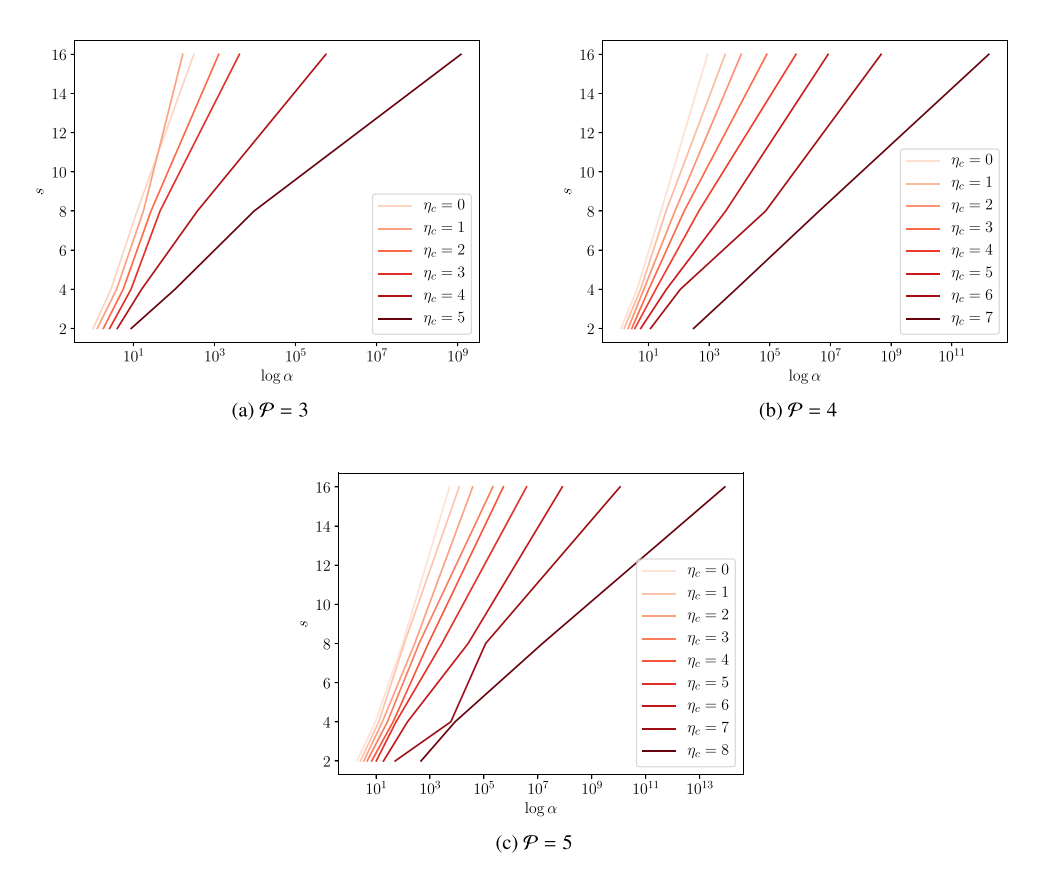


Fig. 31. Plots of stability for different  $\mathcal{P}$ 's at  $\Lambda_{Mach=0.2}$ .

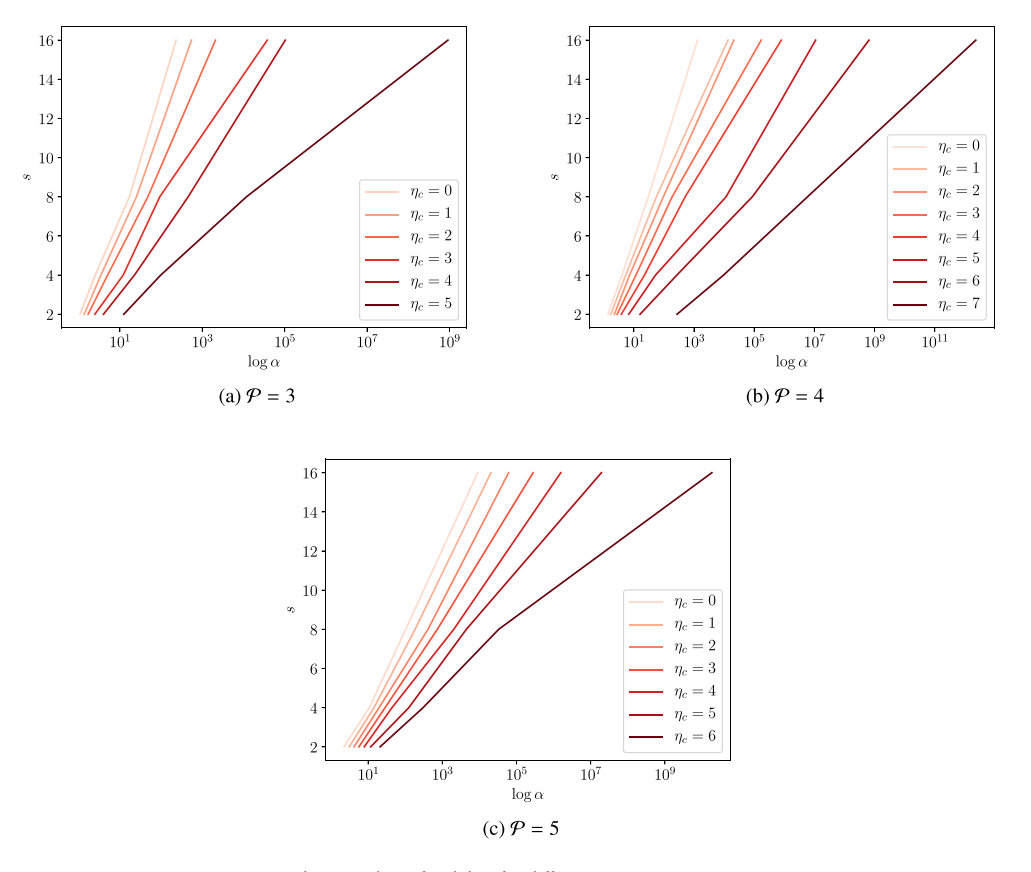


Fig. 32. Plots of stability for different  $\mathcal{P}$ 's at  $\Lambda_{Mach=0.3}$ .

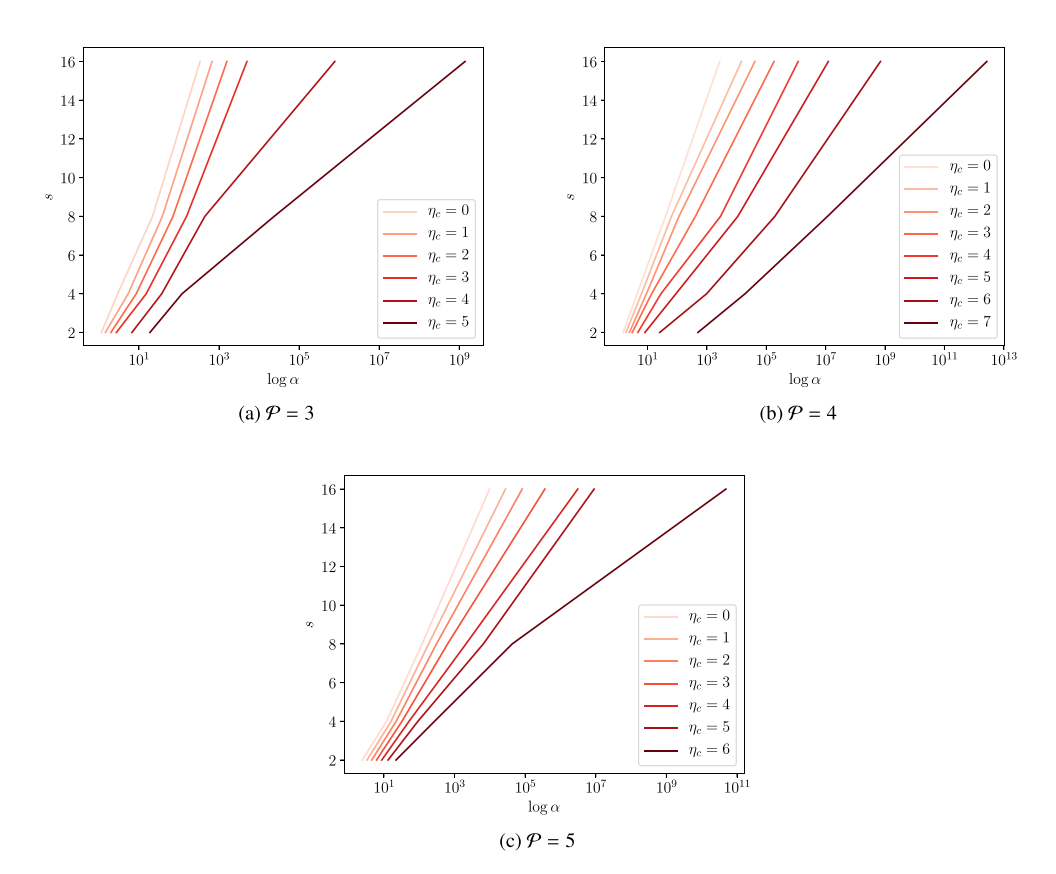


Fig. 33. Plots of stability for different  $\mathcal{P}$ 's at  $\Lambda_{Mach=0.4}$ .

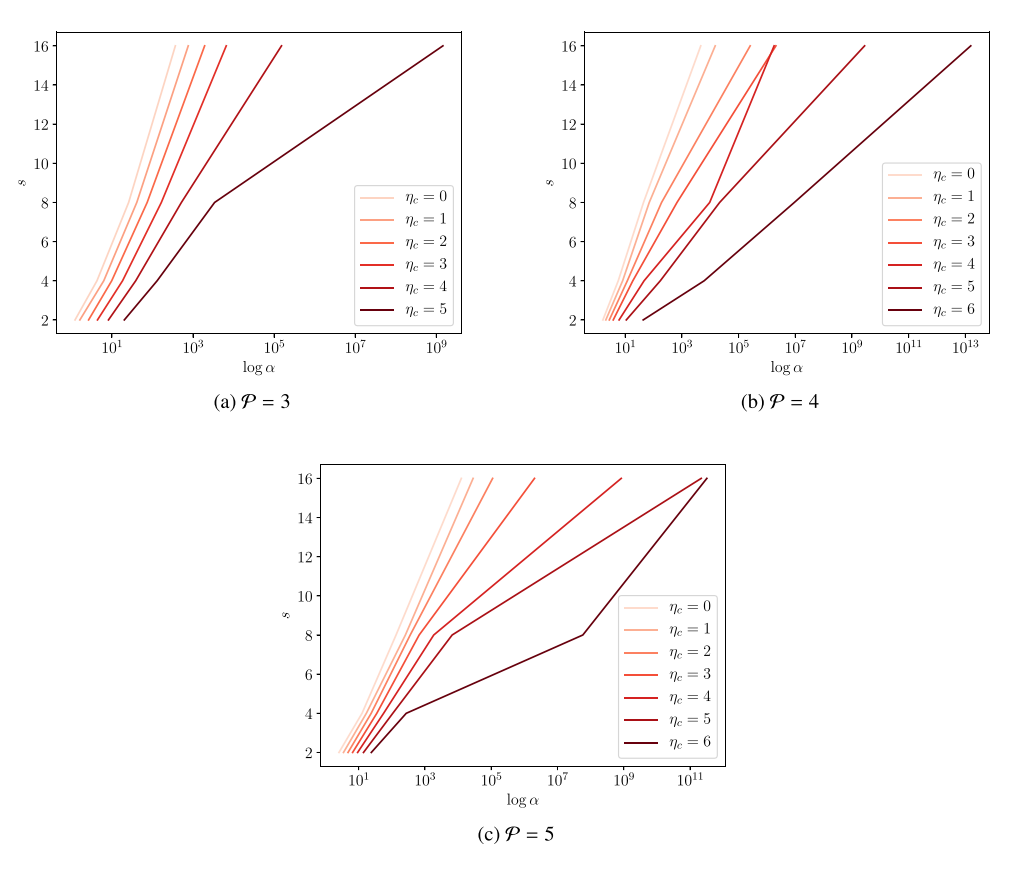


Fig. 34. Plots of stability for different  $\mathcal{P}$ 's at  $\Lambda_{Mach=0.5}$ .

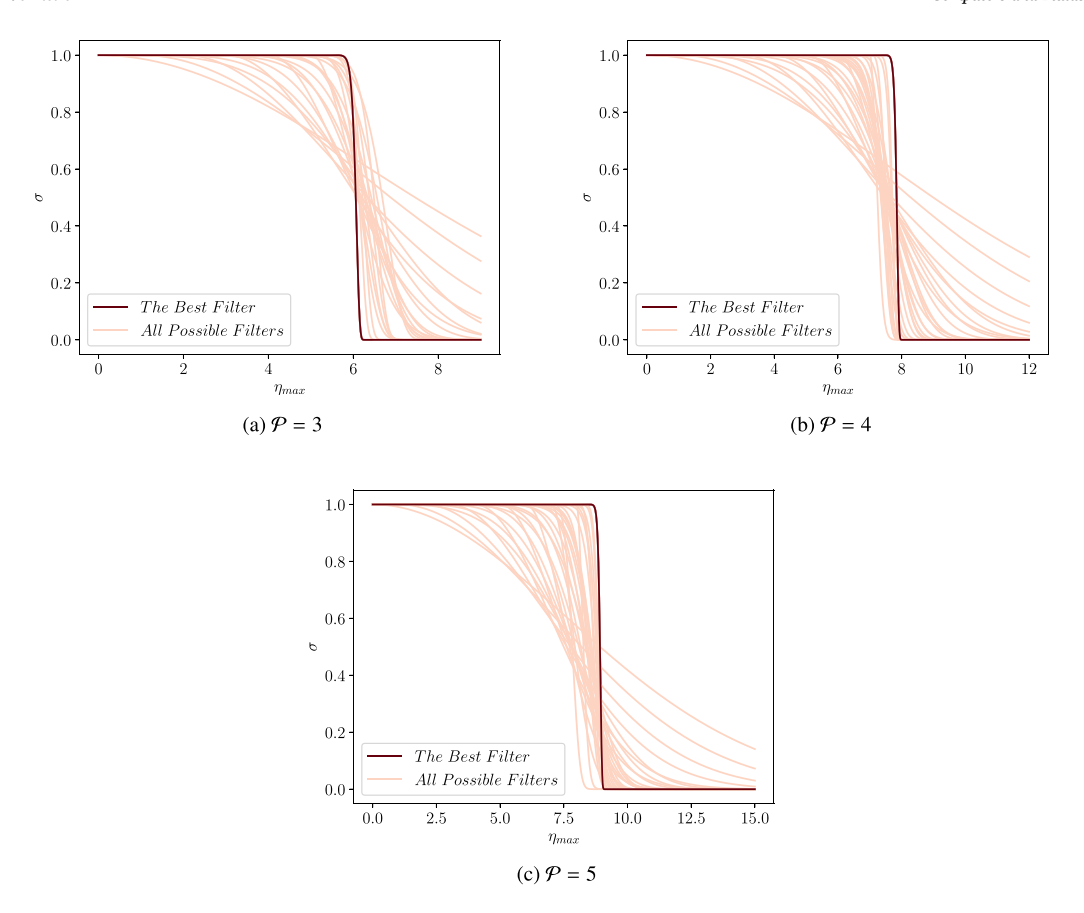


Fig. 35. Plots of all possible filter functions for different  $\mathcal{P}$ 's and the best one at  $\Lambda_{Mach=0.2}$ .

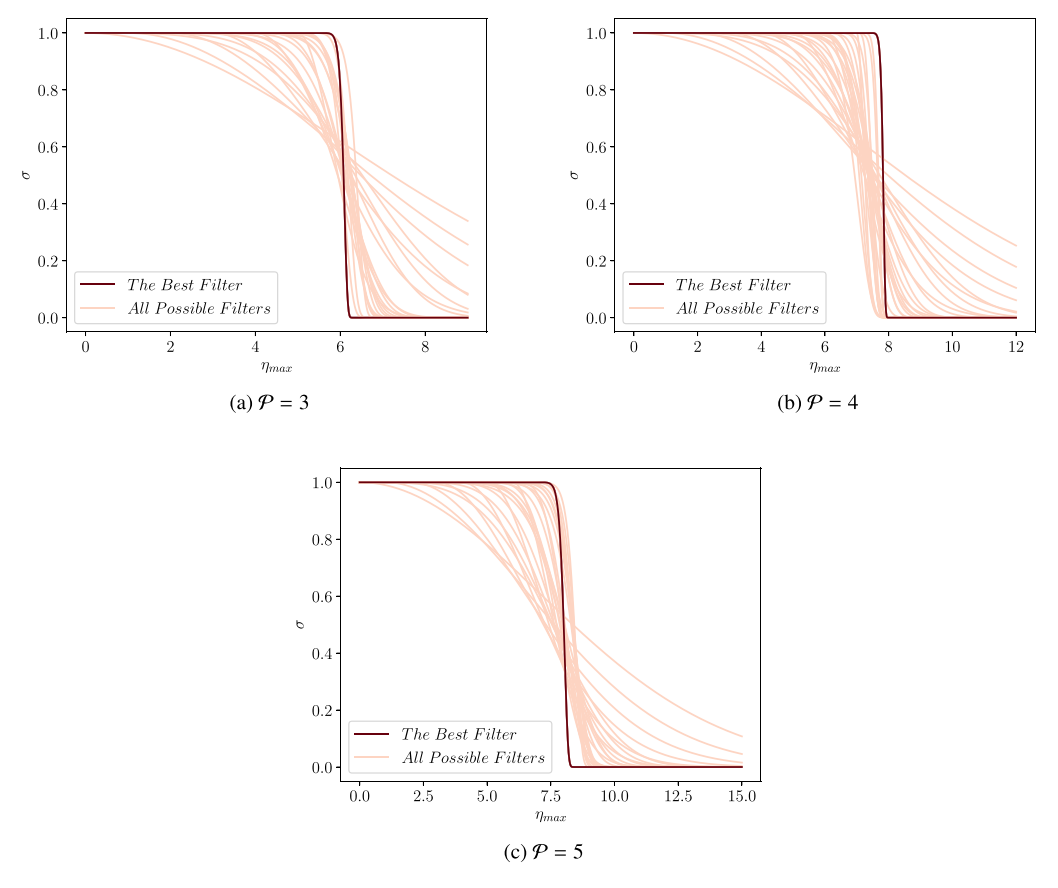


Fig. 36. Plots of all possible filter functions for different  $\mathcal{P}$ 's and the best one at  $\Lambda_{Mach=0.3}$ .

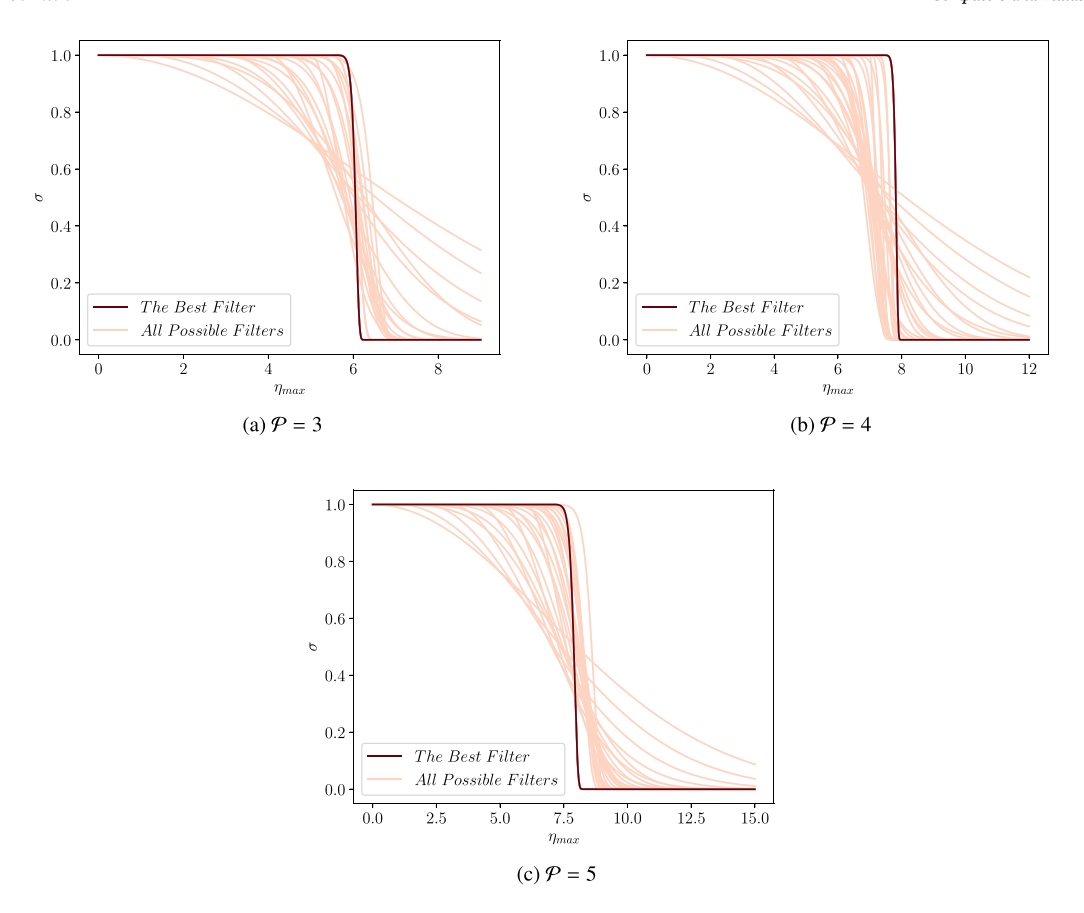


Fig. 37. Plots of all possible filter functions for different  $\mathcal{P}$ 's and the best one at  $\Lambda_{Mach=0.4}$ .

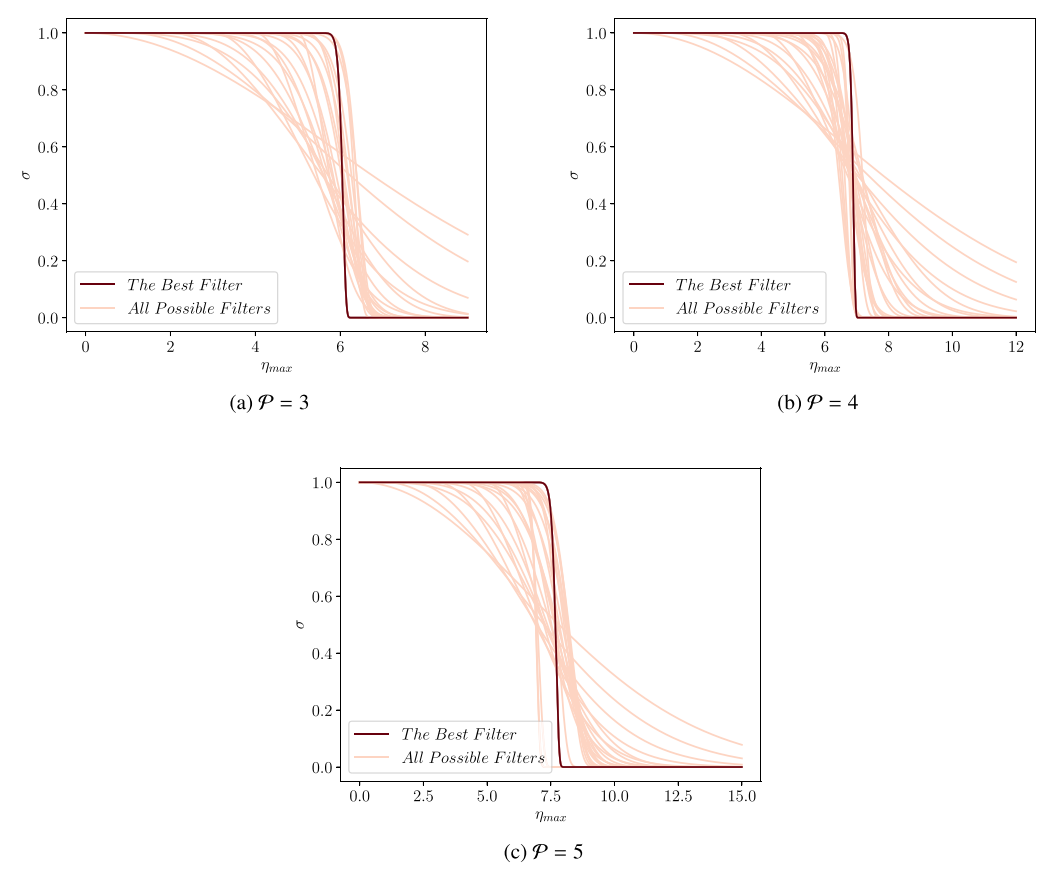


Fig. 38. Plots of all possible filter functions for different  $\mathcal{P}$ 's and the best one at  $\Lambda_{Mach=0.5}$ .

#### References

- [1] Slotnick Jeffrey, Khodadoust Abdollah, Alonso Juan, Darmofal David, Gropp William, Lurie Elizabeth, et al. CFD vision 2030 study: A path to revolutionary computational aerosciences. 2014.
- [2] Vincent Peter, Witherden Freddie, Vermeire Brian, Park Jin Seok, Iyer Arvind. Towards green aviation with Python at petascale. In: Proceedings of the international conference for high performance computing, networking, storage and analysis. IEEE Press; 2016, p. 1.
- [3] Vermeire Brian C, Witherden Freddie D, Vincent Peter E. On the utility of GPU accelerated high-order methods for unsteady flow simulations: A comparison with industry-standard tools. J Comput Phys 2017;334:497–521.
- [4] Langguth Johannes, Wu Nan, Chai Jun, Cai Xing. On the GPU performance of cell-centered finite volume method over unstructured tetrahedral meshes. In: Proceedings of the 3rd workshop on irregular applications: architectures and algorithms. ACM; 2013, p. 7.
- [5] Spiegel Seth C, Huynh HT, DeBonis James R. De-aliasing through over-integration applied to the flux reconstruction and discontinuous Galerkin methods. In: 22nd AIAA computational fluid dynamics conference. 2015, p. 2744.
- [6] Sandham ND, Reynolds WC. Three-dimensional simulations of large eddies in the compressible mixing layer. J Fluid Mech 1991;224:133–58.
- [7] Kim Jae Wook, Lee Duck Joo. Optimized compact finite difference schemes with maximum resolution. AIAA J. 1996;34(5):887–93.
- [8] Chung Yongmann M, Tucker Paul G. Accuracy of higher-order finite difference schemes on nonuniform grids. AIAA J 2003;41(8):1609–11.
- [9] Guermond Jean-Luc, Popov Bojan. Invariant domains and second-order continuous finite element approximation for scalar conservation equations. SIAM J Numer Anal 2017;55(6):3120–46.
- [10] Chavent Guy, Cockburn Bernardo. The local projection discontinuous Galerkin finite element method for scalar conservation laws. ESAIM: Math Model Numer Anal 1989;23(4):565–92.
- [11] Chavent Guy, Salzano G. A finite-element method for the 1-d water flooding problem with gravity. J Comput Phys 1982;45(3):307–44.
- [12] Reed William H, Hill TR. Triangular mesh methods for the neutron transport equation. Technical report, Los Alamos Scientific Lab., N. Mex.(USA); 1973.
- [13] Cockburn Bernardo, Shu Chi-Wang. The runge-kutta local projection discontinuous Galerkin finite element method for scalar conservation laws. ESAIM: Math Model Numer Anal 1991;25(3):337–61.
- [14] Cockburn Bernardo, Shu Chi-Wang. TVB Runge-Kutta Local projection discontinuous Galerkin finite element method for conservation laws II: general framework. Math Comput 1989;52(186):411–35.
- [15] Cockburn Bernardo, Lin San-Yih, Shu Chi-Wang. TVB Runge-Kutta Local projection discontinuous Galerkin finite element method for conservation laws III: one-dimensional systems. J Comput Phys 1989;84(1):90–113.
- [16] Cockburn Bernardo, Hou Suchung, Shu Chi-Wang. The Runge-Kutta local projection discontinuous Galerkin finite element method for conservation laws IV: the multidimensional case. Math Comput 1990;54(190):545–81.
- [17] Cockburn Bernardo, Shu Chi-Wang. The Runge-Kutta discontinuous Galerkin method for conservation laws v: multidimensional systems. J Comput Phys 1998;141(2):199-224.
- [18] Kopriva David A, Kolias John H. A conservative staggered-grid Chebyshev multidomain method for compressible flows. J Comput Phys 1996;125(1):244– 61
- [19] Liu Yen, Vinokur Marcel, Wang Zhi Jian. Spectral difference method for unstructured grids I: basic formulation. J Comput Phys 2006;216(2):780-801.
- [20] Wang Zhi Jian, Liu Yen, May Georg, Jameson Antony. Spectral difference method for unstructured grids II: extension to the Euler equations. J Sci Comput 2007;23(1):45-71.
- [21] Wang Zhi Jian. Spectral (finite) volume method for conservation laws on unstructured grids: basic formulation. J Comput Phys 2002;178(1):210–51.
- [22] Huynh Hung T. A flux reconstruction approach to high-order schemes including discontinuous Galerkin methods. In: 18th AIAA computational fluid dynamics conference. 2007, p. 4079.
- [23] Zwanenburg Philip, Nadarajah Siva. Equivalence between the energy stable flux reconstruction and filtered discontinuous Galerkin schemes. J Comput Phys 2016;306;343–69.
- [24] Vermeire Brian C, Vincent Peter E. On the properties of energy stable flux reconstruction schemes for implicit large eddy simulation. J Comput Phys 2016;327:368–88.
- [25] Vermeire Brian C, Nadarajah Siva, Tucker Paul G. Implicit large eddy simulation using the high-order correction procedure via reconstruction scheme. Int J Numer Methods Fluids 2016;82(5):231–60.
- [26] Pereira Carlos A, Vermeire Brian C. Spectral properties of high-order element types for implicit large eddy simulation. J Sci Comput 2020;85(2):1–38.
- [27] Vermeire Brian, Cagnone Jean-Sebastien, Nadarajah Sivakumaran. ILES using the correction procedure via reconstruction scheme. In: 51st AIAA aerospace sciences meeting including the new horizons forum and aerospace exposition. 2013, p. 1001.

- [28] Vermeire Brian C, Nadarajah Sivakumaran, Tucker Paul G. Canonical test cases for high-order unstructured implicit large eddy simulation. In: 52nd aerospace sciences meeting. 2014, p. 0935.
- [29] Wang Zhijian J, Fidkowski Krzysztof, Abgrall Rémi, Bassi Francesco, Caraeni Doru, Cary Andrew, et al. High-order CFD methods: current status and perspective. Int J Numer Methods Fluids 2013;72(8):811–45.
- [30] Witherden Freddie D, Vermeire Brian C, Vincent Peter E. Heterogeneous computing on mixed unstructured grids with PyFR. Comput & Fluids 2015;120:173–86.
- [31] Haga Takanori, Tsutsumi Seiji, Kawai Soshi, Takaki Ryoji. Large-eddy simulation of a supersonic jet using high-order flux reconstruction scheme. In: 53rd AIAA aerospace sciences meeting, 2015, p. 0831.
- [32] Pereira Carlos A, Vermeire Brian C. Fully-discrete analysis of high-order spatial discretizations with optimal explicit Runge-Kutta methods. J Sci Comput 2020;83(3):1-35.
- [33] Vermeire BC, Vincent PE. On the behaviour of fully-discrete flux reconstruction schemes. Comput Methods Appl Mech Eng 2017;315:1053–79.
- [34] Phillips Norman A. An example of non-linear computational instability. 501, Rockefeller Institute Press New York; 1959, p. 504.
- [35] Kirby Robert M, Karniadakis George Em. De-aliasing on non-uniform grids: algorithms and applications. J Comput Phys 2003;191(1):249–64.
- [36] Jameson Antony, Vincent Peter E, Castonguay Patrice. On the non-linear stability of flux reconstruction schemes. J Sci Comput 2012;50(2):434–45.
- [37] Rojas Diego, Boukharfane Radouan, Dalcin Lisandro, Fernández David C Del Rey, Ranocha Hendrik, Keyes David E, et al. On the robustness and performance of entropy stable collocated discontinuous Galerkin methods. J Comput Phys 2021;426:109891.
- [38] Persson Per-Olof, Peraire Jaime. Sub-cell shock capturing for discontinuous Galerkin methods. In: 44th AIAA aerospace sciences meeting and exhibit. 2006, p. 112.
- [39] VonNeumann John, Richtmyer Robert D. A method for the numerical calculation of hydrodynamic shocks. J Appl Phys 1950;21(3):232–7.
- [40] Burbeau Anne, Sagaut Pierre, Bruneau Ch-H. A problem-independent limiter for high-order Runge-Kutta discontinuous Galerkin methods. J Comput Phys 2001;169(1):111–50.
- [41] Trojak William, Watson Robert, Tucker Paul G. Temporal stabilisation of flux reconstruction on linear problems. In: 2018 fluid dynamics conference. 2018, p. 4263
- [42] Park JS, Witherden FD, Vincent PE. High-order implicit large-eddy simulations of flow over a NACA0021 aerofoil. AIAA J 2017;2186–97.
- [43] Hesthaven Jan S, Warburton Tim. Nodal discontinuous galerkin methods: algorithms, analysis, and applications. Springer Science & Business Media; 2007.
- [44] Mengaldo Gianmarco, De Grazia Daniele, Moxey David, Vincent Peter E, Sher-win Spencer J. Dealiasing techniques for high-order spectral element methods on regular and irregular grids. J Comput Phys 2015;299:56–81.
- [45] Wang Zhi Jian, Gao Haiyang. A unifying lifting collocation penalty formulation including the discontinuous Galerkin, spectral volume/difference methods for conservation laws on mixed grids. J Comput Phys 2009;228(21):8161–86.
- [46] Asthana Kartikey, López-Morales Manuel R, Jameson Antony. Non-linear stabilization of high-order flux reconstruction schemes via Fourier-spectral filtering. J Comput Phys 2015;303:269–94.
- [47] Moura Rodrigo C, Mengaldo Gianmarco, Peiró Joaquim, Sherwin Spencer J. On the eddy-resolving capability of high-order discontinuous Galerkin approaches to implicit LES/under-resolved DNS of Euler turbulence. J Comput Phys 2017;320:615-22
- [48] Mengaldo Gianmarco, De Grazia Daniele, Vincent Peter E, Sherwin Spencer J. On the connections between discontinuous Galerkin and flux reconstruction schemes: extension to curvilinear meshes. J Sci Comput 2016;67(3):1272–92.
- [49] Hesthaven Jan, Kirby Robert. Filtering in Legendre spectral methods. Math Comput 2008;77(263):1425–52.
- [50] Blackburn Hugh M, Schmidt S. Spectral element filtering techniques for large eddy simulation with dynamic estimation. J Comput Phys 2003;186(2):610–29.
- [51] Hou Thomas Y, Li Ruo. Computing nearly singular solutions using pseudospectral methods. J Comput Phys 2007;226(1):379–97.
- [52] Witherden Freddie D, Farrington Antony M, Vincent Peter E. PyFR: An open source framework for solving advection-diffusion type problems on streaming architectures using the flux reconstruction approach. Comput Phys Comm 2014;185(11):3028–40.
- [53] Bull Jonathan R, Jameson Antony. Simulation of the Taylor–Green vortex using high-order flux reconstruction schemes. AIAA J 2015;53(9):2750–61.
- [54] Bull Jonathan R, Jameson Antony. Simulation of the compressible Taylor–Green vortex using high-order flux reconstruction schemes. In: 7th AIAA theoretical fluid mechanics conference. 2014, p. 3210.
- [55] Chapelier Jean-Baptiste, De La Llave Plata Marta, Renac Florent. Inviscid and viscous simulations of the Taylor-Green vortex flow using a modal discontinuous Galerkin approach. In: 42nd AIAA fluid dynamics conference and exhibit. 2012, p. 2072
- [56] Chapelier J-B, De La Llave Plata Marta, Lamballais Eric. Development of a multiscale LES model in the context of a modal discontinuous Galerkin method. Comput Methods Appl Mech Eng 2016;307:275–99.

- [57] Johnsen Eric, Varadan Sreenivas, Van Leer Bram. A three-dimensional recovery-based discontinuous Galerkin method for turbulence simulations. In: 51st AIAA aerospace sciences meeting including the new horizons forum and aerospace exposition. 2013, p. 515.
- [58] Gassner Gregor J, Beck Andrea D. On the accuracy of high-order discretizations for underresolved turbulence simulations. Theor Comput Fluid Dyn 2013;27(3-4):221-37.
- [59] Diosady Laslo Tibor, Murman Scott M. Design of a variational multiscale method for turbulent compressible flows. 2013.
- [60] Alhawwary Mohammad A, Wang Zhi J. Comparative Fourier analysis of DG, FD and compact difference schemes. In: 2018 fluid dynamics conference. 2018, p. 4267
- [61] Van Rees Wim M, Leonard Anthony, Pullin Dale I, Koumoutsakos Petros. A comparison of vortex and pseudo-spectral methods for the simulation of periodic vortical flows at high Reynolds numbers. J Comput Phys 2011;230(8):2794–805.
- [62] Navah Farshad, Plata Marta de la Llave, Couaillier Vincent. A high-order variational multiscale approach to turbulence for compact nodal schemes. 2018, arXiv preprint arXiv:1809.03966.
- [63] Abe Yoshiaki, Haga Takanori, Nonomura Taku, Fujii Kozo. Conservative highorder flux-reconstruction schemes on moving and deforming grids. Comput & Fluids 2016;139:2–16.
- [64] Trojak Will, Watson Rob, Scillitoe Ashley, Tucker Paul G. Effect of mesh quality on flux reconstruction in multi-dimensions. J Sci Comput 2020;82(3):1–36.
- [65] Kim John, Moin Parviz, Moser Robert. Turbulence statistics in fully developed channel flow at low Reynolds number. J. Fluid Mech. 1987;177:133–66.
- [66] Abe Hiroyuki, Kawamura Hiroshi, Matsuo Yuichi. Direct numerical simulation of a fully developed turbulent channel flow with respect to the Reynolds number dependence. J Fluids Eng 2001;123(2):382–93.
- [67] Vermeire Brian C. Paired explicit Runge-Kutta schemes for stiff systems of equations. J Comput Phys 2019;393:465–83.
- [68] Rosti Marco E, Omidyeganeh Mohammad, Pinelli Alfredo. Direct numerical simulation of the flow around an aerofoil in ramp-up motion. Phys Fluids 2016;28(2):025106.